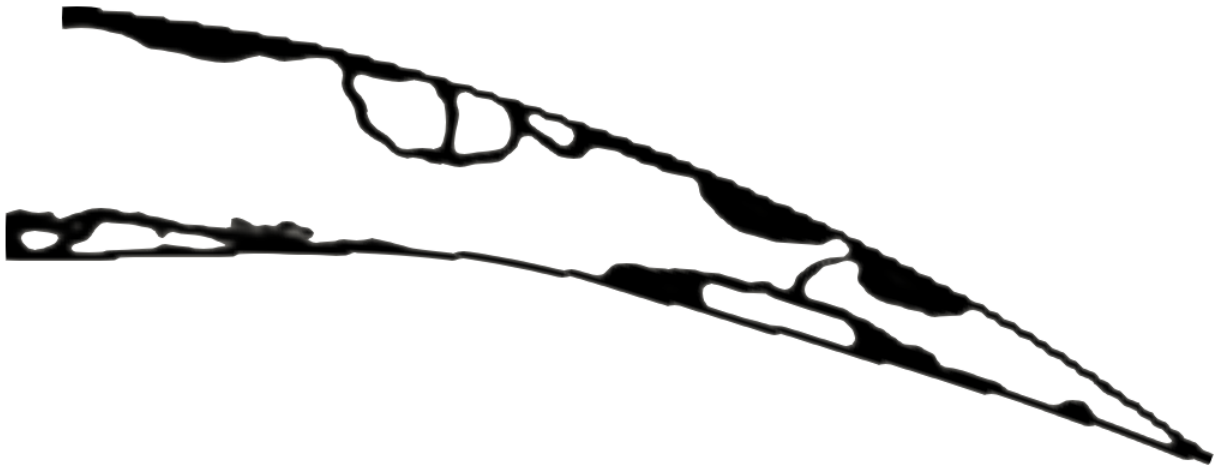


## Department of Precision and Microsystems Engineering

### The topology optimization of a compliant variable-camber morphing wing

J.W. Maas

Report no : 2021.047  
Coach : Stijn Koppen, Msc  
Professor : Prof. Dr. Ir. Fred van Keulen  
Specialisation : Engineering Mechanics  
Type of report : Master Thesis  
Date : August 2, 2021





# The topology optimization of a compliant variable-camber morphing wing

by

J.W. Maas

to obtain the degree of Master of Science  
at the Delft University of Technology,  
to be defended publicly on Tuesday, August 17, 2021 at 14.00.

Student number:	4377125	
Project duration:	June, 2020 – August, 2021	
Thesis committee:	Prof. dr. ir. F. Van Keulen,	TU Delft, supervisor
	S. Koppen, MSc,	TU Delft, supervisor
	Prof. dr. ir. G. Schitter,	TU Vienna, supervisor
	A. Galffy, Msc,	TU Vienna, supervisor
	Dr. ir. M. Tichem,	TU Delft, committee member

*This thesis is confidential and cannot be made public until august 17, 2022.*

An electronic version of this thesis is available at <http://repository.tudelft.nl/>.



# Preface

Before you lies my master thesis 'The topology optimization of a compliant variable-camber morphing wing', that describes a new approach for the design of a variable-camber morphing wing. It has been written to fulfil the program of the track High-Tech Engineering within the master Mechanical Engineering at the Delft University of Technology. The project was a collaboration with the Technical University of Vienna.

I would like to thank my supervisors from the TU Delft, Fred van Keulen and Stijn Koppen. Thank you for your enthusiastic and active guidance during the project and for coping with my endless stream of questions. Our regular meetings and discussions of the material were a key ingredient in keeping me on track and increase my understanding of the subject matter. I would also like to thank Georg Schitter and Andras Galffy from TU Vienna for their involvement in the project and their active feedback during the course of it. Unfortunately, I was unable to come to Vienna for part of the project due to the Covid-19 pandemic, but hopefully I will still be able to meet you in person in the future.

Each project has its setbacks and this one was no exception to that rule. I would not have been able to achieve it without the support and help of my friends and family. I would like to thank Eveline Matroos, our amazing master coordinator at High-Tech Engineering, for her help, guidance and positivity during the course of my masters. I also would like to thank my parents, who have always supported me and helped me through everything. Thank you for motivating me and for your unwavering support. A special shout-out to my sister, Dorien, who took time out of her busy post-doc schedule to provide me with feedback on my thesis and who was always there for me when I needed her. Finally, thank you to all my friends, in and outside of Delft, who helped keep me motivated and provided me with (positive) distractions when I needed them. Now, on to the next adventure!

Wietske Maas

July, 2021



# Abstract

In aeronautics, the camber variation of the airfoil profile of the wing is an important means of flight control as it is used to generate high lift coefficients during take-off and landing. In conventional aircrafts, lift control is achieved by using flap systems. However, conventional flap systems contain discontinuous sections that cause aerodynamic losses. It would therefore be beneficial if flap systems could be replaced by a variable-camber morphing wing. It has been shown that variable-camber morphing wings can significantly improve the aerodynamic performance of the aircraft due to the smoothness of the surface, making it possible to fly more efficiently, reduce fuel consumption and reduce the impact on the environment. However, the design of such a variable-camber morphing wing is challenging due to the conflicting requirements of the structure. The wing should be flexible so it can morph, stiff so it can withstand aerodynamic pressures and light weight to reduce fuel consumption.

The aim of this work is to provide a method for the density-based topology optimization of compliant morphing structures. The method includes a novel formulation for the objective function which compares the deformed shape of the structure with a desired deformed shape by using a dot product. This dot-product objective proved to be more capable of realising shape morphing structures which obtained their desired output shapes than the commonly used least-squares-error objective does. The dot-product objective converges to an optimum better than the least-squares-error objective does. For even a relatively simple optimization with up to 500 variables the dot-product found the optimum roughly 15 times as fast as the least squares error objective did. The developed method is applied to obtain an optimized design of a compliant variable-camber morphing wing. The dot-product objective aims to optimize the structure for a quadratic output shape of the top surface of the trailing edge. The skin of the airfoil profile is included in this optimization as a non-design domain and not considered a separate structure. By using the dot-product objective function, the optimization yielded a design which was able to obtain a quadratic shape of the deformed top-surface of the trailing edge, while also complying with the constraints on flexibility, stiffness and mass of the structure.

The obtained design was converted to a prototype by 3D printing and an experiment was performed to assess if the deformed shapes of the prototype were similar to the ones predicted by the analysis in the topology optimization. The experiment showed that for small deformations the output shape matched the predicted output shape. For larger deflections, there was a slight difference. However, the obtained shapes were still quadratic-like and so it is expected that for larger deformations the designed trailing edge will still have superior aerodynamic performance than conventional flap systems.

In conclusion, the proposed density-based topology optimization with a dot-product objective function is able to obtain structures which comply well with desired shape changes. This was also shown in the designed variable-camber morphing wing, which is able to obtain the desired quadratic shape when deformed, while also complying with the constraints.



# Contents

<b>1</b>	<b>Introduction</b>	<b>1</b>
1.1	Compliant mechanisms . . . . .	2
1.2	Structural optimization . . . . .	3
1.3	State-of-the-art of the topology optimization of variable-camber morphing wings . . . . .	4
<b>2</b>	<b>Methods</b>	<b>7</b>
2.1	Modelling assumptions for compliant shape-morphing structures . . . . .	7
2.2	Analysis of the obtained structure within each iteration . . . . .	8
2.3	Sensitivities . . . . .	9
<b>3</b>	<b>Objective function investigation</b>	<b>11</b>
3.1	Shape-adaptable surface mechanisms with a LSE objective function . . . . .	11
3.2	Comparison LSE and dot-product objective function for a shape-adaptable surface mechanism	15
3.3	A minimum working example . . . . .	16
<b>4</b>	<b>Numerical examples</b>	<b>21</b>
4.1	The design problem of a variable-camber morphing wing . . . . .	21
4.2	The influence of element densities on expected deformations . . . . .	24
4.3	Final design . . . . .	27
<b>5</b>	<b>Experimental validation</b>	<b>31</b>
<b>6</b>	<b>Conclusions and recommendations</b>	<b>33</b>
6.1	Conclusions . . . . .	33
6.2	Recommendations for future research . . . . .	34
<b>A</b>	<b>Matlab code</b>	<b>38</b>
<b>B</b>	<b>Eigenfrequency analysis</b>	<b>44</b>
<b>C</b>	<b>Experimental images</b>	<b>46</b>



# Chapter 1

## Introduction

In aeronautics, the camber of an airfoil is a measure of the curvature of the airfoil. It is the asymmetry between the curvature of the top- and bottom surface [1]. Camber variation of the airfoil profile of a wing is an important means of control in aircrafts as it is used to generate high lift coefficients during take-off and landing [2]. In conventional aircrafts, lift control is achieved by using flap systems. However, conventional flap systems contain discontinuous sections that cause aerodynamic losses [3]. Therefore, it would be beneficial if these systems could be replaced by a morphing wing. The term morphing refers to seamless shape changes that are continuous. A morphing wing would therefore not rely on the movement of discrete parts, but rather consist of one continuously deforming structure that can change its shape to fit the conditions present during flight [4] [5]. There are different types of morphing wings concerned with different parameters such as span, sweep, twist and camber. For the purpose of lift control, a variable-camber morphing wing is needed [6]. In a variable-camber morphing wing, the flaps will be replaced by an airfoil section that can change its camber due to shape morphing of the structure (see Fig. 1.1). It has been shown that this can significantly improve the aerodynamic performance of the wing due to the smoothness of the surface [7]. The morphing wing can increase the lift with a very low drag-penalty, making it possible to fly more efficiently, reduce fuel consumption and reduce the impact on the environment.

The main requirements in a variable-camber morphing wing design are that the structure should be flexible so it can morph, stiff so it can withstand aerodynamic pressures and light weight to reduce fuel consumption [9]. The challenge is that these three properties are inherently contradictory. In order to stiffen a structure, one usually adds material which can be problematic if a structure needs to be light weight. Furthermore, when one stiffens a structure one inherently loses flexibility and yet a morphing wing requires both of these qualities. These three properties together make a variable-camber morphing wing a challenging design problem. In this thesis, the focus will be on the design of a morphing trailing edge that could replace trailing edge-flap systems as they are applied in modern conventional aircrafts. The leading edge will not be considered in the design.

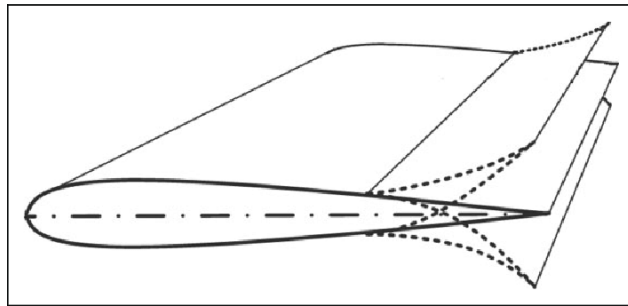


Figure 1.1: A variable-camber morphing wing, with a morphing trailing edge. The dashed lines represent the morphed configuration of the wing. In these morphed configurations, the top and bottom surface remain smooth, and do not contain any sharp corners [8].

Various structures such as lattice structures, multi-stable structures and compliant structures have been researched for applicability in a variable-camber morphing wing. For an overview of the research in this area, take a look at reviews such as Barbarino, Bilgen, Ajaj, *et al.* [5] and Sun, Guan, Liu, *et al.* [10]. Of these structures, compliant mechanisms seem to offer many advantages. In the next Section, compliant mechanisms and their possible applicability to a variable-camber morphing wing are discussed.

## 1.1 Compliant mechanisms

A compliant mechanism is defined as a monolithic structure that achieves a desired deformed shape by elastic deformation within the structure [11]. This means no discrete elements such as hinges are necessary. This has many advantages such as eliminating backlash error and reducing maintenance as well as assembly costs. Additionally, compliant mechanisms can also create a more smooth and evenly distributed deformation than their rigid body counterparts [11]. These properties make compliant structures an interesting candidate for the design of a variable-camber morphing wing.

A compliant mechanism can rely on different types of compliance, which are generally divided into two groups: lumped compliance and distributed compliance. Compliance is here referred to as the way in which a mechanism elastically deforms. Mechanisms with lumped compliance essentially are conventional, rigid body mechanisms in which the hinges are replaced by solid-state hinges. A solid-state hinge is a short-length region with a reduced thickness and therefore a low bending stiffness [12]. While this type of compliance yields mechanisms with clearly defined kinematics, they also imply poor load-carrying capability. Mechanisms with distributed compliance can avoid this problem [12]. In distributed compliant mechanisms, long-length pivots are used to produce smooth changes of the geometry [13]. This results in reduced stress concentrations within the structure. The behaviour of a distributed compliant mechanism is mainly load dependent, i.e. different deformation patterns can be obtained by changing the loads acting on the mechanism [13]. Since part of the loads are not controllable, this can negatively influence the systems reliability and precision. Hasse *et al* [14] introduce a third group of compliance: selective compliance. Selective compliant mechanisms enable smooth shape changes by keeping a high degree of stiffness in other deformation components. This implies that the mechanisms will be flexible with respect to the deformation it was designed for, while being stiff with respect to other deformation modes. Selective compliance combines the advantages of both lumped and distributed compliance, namely reduced stress concentrations, a smooth deformation pattern and defined kinematics. This is also what is aimed for in a variable-camber morphing wing: a smooth deformation pattern with a high degree of stiffness in other directions.

To further classify the compliant variable-camber morphing wing, it should be noted that there are three different types of compliant mechanisms: the path generator, the function generator and the motion generator. Cao, Dolovich, and Zhang [15] define these different types of mechanisms as follows. (1) A path generator is a mechanism in which a point is controlled such that it follows a prescribed path. (2) A function generator is a mechanism in which there is a correlation of an input motion with an output motion. (3) A motion generator is a mechanism in which the goal is to design a mechanism which can guide a (flexible) segment from an original configuration to a desired morphed configuration [5], see Fig. 1.2.

A compliant variable-camber morphing wing can be classified as a motion generating compliant mechanism. Compliant motion generators can be designed through structural optimization. This is an interesting technique for designing such a mechanism especially when the design problem is complex, which is the case for a variable-camber morphing wing. This complexity makes the result of this design problem dependent on the experience of the designer and creates difficulty in finding an optimal solution. Therefore, a structural optimization of the design problem would be a powerful tool. Structural optimization will be further discussed in the next Section.

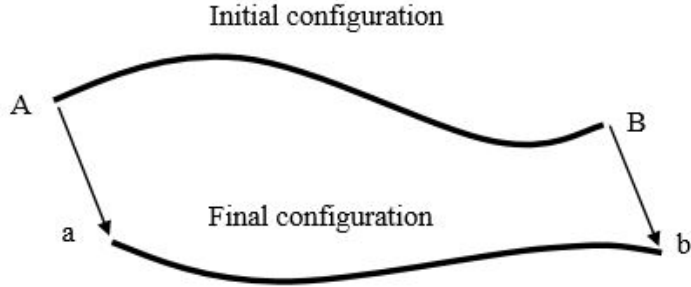


Figure 1.2: Representation of the goal of a flexible motion-generator. The goal is to design a mechanism which can convert the segment from the original configuration (AB) into the final, morphed configuration (ab). [15].

## 1.2 Structural optimization

Structural optimization is the design method which involves an optimization of a specific performance measure of the structure (for example maximize stiffness or minimize mass under a certain load system), while including the constraints which inevitably must be imposed on the structure to satisfy the requirements. The motivation to use structural optimization, or just optimization in general, is to exploit limited resources in such a way that the output or profit is maximized [16].

There are three different types of structural optimization: sizing optimization, shape optimization and topology optimization [17]. Each of these classes address different aspects of the structural design problem. In a typical sizing optimization problem, the design variables are some type of structural thickness, e.g. cross-sectional area of truss members or the thickness distribution of a plate (see Fig. 1.3a), while the initial structure is assumed [18]. In a shape optimization problem the goal is to find the optimum shape of this design domain. A number of topological properties is assumed (e.g. a fixed number of holes) and their shape is optimized (see Fig. 1.3b) [17]. Topology optimization of solid structures involves the determination of features such as the number, shape and location of holes and the connectivity within a predefined design domain [17]. For the design of the compliant variable-camber morphing wing, topology optimization is suggested in literature as a design approach [19].

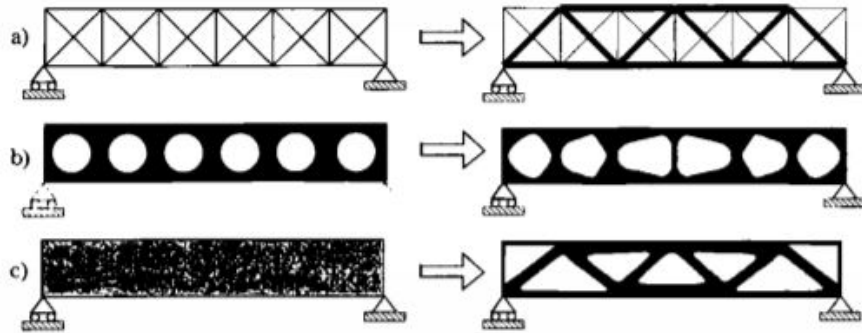


Figure 1.3: The three categories of structural optimization. a) Sizing optimization: an initial structure is assumed, the sizes are determined by the optimization. b) Shape optimization: a number of holes is prescribed, the shape of these holes is optimized. c) Topology optimization: the generation of a structure within a specified domain. [17].

A topology optimization is based on the principle of removing and adding material in a design domain. This design domain is discretized into finite elements. Typically, the design variables in a topology optimization are the density  $x$  of element  $e$ ,  $x_e$ . Where:

$$0 \leq x_e \leq 1.$$

During the optimization, this density value is used to interpolate the Young’s modulus of the element. This implies that a density  $x_e = 0$  indicates the absence of material, these elements are called void elements. When  $x_e = 1$  there is material present in the element. It should be noted that in reality there is always material present in an element, it is the Young’s modulus of the element ( $E_e$ ) that is the variable and dependent on the density of that element according to  $E_e = \rho(x_e)E$ , where  $\rho(x_e)$  is the design function which often includes some type of filtering of the design variables, and  $E$  is the Young’s modulus of the chosen material.

The optimization itself is an iterative process in which the values of the design variables are updated at every iteration. Within each iteration, an analysis of the obtained structure for the current density distribution is performed. This is necessary because the estimation of the performance of the structure is only locally valid. That is to say, for every new density distribution the behaviour of the structure will be different and needs to be analyzed. The optimizer that will be used for this process is the Method of Moving Asymptotes (MMA) [20]. MMA is a gradient based optimizer that uses the sensitivities of the objective and constraint functions to update the design variables. MMA is often used in topology optimization and has proven to be reliable in combination with multiple complex, non-linear constraints [21].

While research has been done in the topology optimization of compliant mechanisms, not much of it is focused on shape-morphing compliant mechanisms. The next section will present the state-of-the-art in the topology optimization of shape-morphing structures and then specifically the topology optimization of compliant variable-camber morphing wings.

### 1.3 State-of-the-art of the topology optimization of variable-camber morphing wings

In the literature, different types of objective functions are proposed for the topology optimization of shape morphing mechanisms. Lu and Kota [22] propose a least-squares error objective in which the obtained deformed surface of the generated mechanism is compared against a prescribed curve. The topology optimization involves a domain parameterization method that utilizes the load path of the structure. The variables are the existence of connections between several nodes within the domain and the cross-sectional dimensions of those connections. The load path parameterization method was also applied to a variable camber trailing edge, however the amount of design variables is limited and this results in a rudimentary design for such a structure [22]. Santer and Pellegrino [23] propose a similar approach for the optimization of a morphing leading edge, which is the front part of the airfoil profile. While it has been shown that this approach works with a limited amount of variables, it also limits the optional outcomes of the optimization to a specific type of structure where nodes are connected through beam elements. This eliminates the possibility of a structure where for example a part of the skin is thickened slightly. By limiting the optimization to these types of structures, there is a risk of eliminating the optimal structure from the possibilities.

Another option is a modified Fourier transformation as an objective function [11]. This objective function is especially applicable in a symmetric setting since this formulation focuses on the change in shape, instead of solely on the exact location of the sampling points.

Hasse and Campanille [24] propose a different approach to the topological optimization of motion generating compliant mechanisms. They formulate an objective based on a modal procedure in which they prescribe the desired deformation mode. This method offers the possibility to decouple the synthesis of the structure from the design of the actuator system. Hasse *et al* [13] used this modal synthesis procedure to design a belt-rib airfoil. The idea of this belt-rib structure is that there is a flexible outer belt. The interior of this belt consists of spokes that connect two points of the belt and thus create some stiffness in the mechanism. However, this method has the same limitation as the methods presented above, namely that the structure is limited to a specific type of mechanism where nodes are connected through beam elements.

Furthermore, research has been done into density-based topology optimization of variable-camber morphing wings. Density-based topology optimization refers to the setting where the variables in the optimization are the densities of the elements. Several studies performed density-based optimization of morphing leading- and trailing-edges in which they included the necessary constraints for stiffness with respect to aerodynamic pressures on the airfoil profile [19], [25], [26]. These optimizations resulted in mechanisms which were able to guide a separate morphing skin into the correct morphed shape. However, designing a separate skin to cover

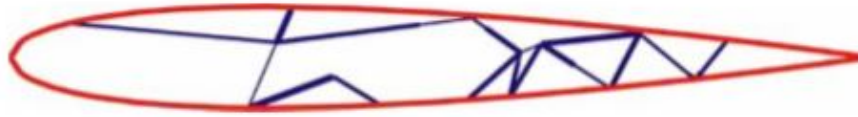


Figure 1.4: The belt-rib variable-camber morphing wing as designed by Hasse *et al* [13]

such morphing structures is a great challenge due to the orthotropic stiffness properties this skin should exhibit (see Thill, Etches, Bond, *et al.* [27] for more information on the morphing skin design problem). Jensen, Wang, Dimino, *et al.* [28] have performed a 3D density-based topology optimization of a variable camber morphing wing. They use a minimal compliance objective, while the desired deformed shape is constrained. The obtained 3D variable-camber morphing wing design was able to comply to desired shape changes reasonably well. While these results show the promise of using density based topology optimization for designing a variable-camber morphing wing, it would be beneficial if the skin could be designed as a part of the compliant mechanism.

In conclusion, some research has been done in the topology optimization of a variable-camber morphing wing. However, often it is not a density-based topology optimization, but a somewhat more limited version with fewer design variables that limit the possible outcomes of the optimization and that result in more rudimentary results of the wing. The obtained designs are often not manufactured and tested. Density-based topology optimization research has been performed and proved to be effective, but the wing skin was seen as a separate mechanism. The designed mechanism was meant to guide this skin into a desired morphed configuration. This adds the problem of designing a morphing skin, which is a challenging design problem.

This thesis presents a method that can be used to perform density-based topology optimization of compliant shape-morphing structures. This includes the definition of a novel objective function definition based on a dot-product, which focuses on the difference in shape between the deformed state and a defined, desired shape. This method is then used to perform density-based topology optimization of a compliant variable-camber morphing wing that, in contrast to previously published work, incorporates the wing skin as part of the compliant mechanism. As such, the model solves both the problem of variable camber as well as the morphing skin design problem. This design was manufactured and used to evaluate the performance of the wing to validate the method.

The remainder of this thesis is set-up as follows. In Chapter 2, the method for the topology optimization of shape-morphing structures is described, including the modelling assumptions made and an explanation of the analysis that happens at every iteration of the optimization. In Chapter 3, the objective function for the optimization will be investigated. In Chapter 4, numerical examples for a variable-camber morphing wing will be discussed and in Chapter 5, the experimental results of a 3D printed prototype of the design will be presented. Finally, in Chapter 6 the conclusions and recommendations for further research will be discussed.



# Chapter 2

## Methods

In this Chapter, an approach for the density-based topology optimization of compliant shape-morphing structures will be discussed. The design problem of morphing structures will be discussed and the modelling assumptions presented in Section 2.1. In Section 2.2, the analysis of the obtained structure that is to be performed in each iteration of the optimization is discussed. In Section 2.3, the method which is used to evaluate the sensitivities that are necessary for the optimization is discussed.

### 2.1 Modelling assumptions for compliant shape-morphing structures

The term morphing refers to seamless shape changes that are continuous. Compliant shape-morphing structures are thus structures that can change their shape by continuously deforming their body [5]. The goal in such a structure is to obtain a prescribed shape from a specified input. This would also be the objective of an optimization of such a structure. In order to quantify how well a morphing structure performs, a function should be developed that can evaluate how well the obtained structure adheres to the required shape changes. This can be done based on the displacement field of the structure in deformed configuration. The displacement of several nodes could be compared with the displacement they should have in the desired shape-morphed state. The set-up of an objective function that can make this comparison in an efficient way is discussed in Chapter 3. This objective function is a key part of the method presented in this thesis, since it determines the performance of the optimization. It is especially important that this objective function performs well in combination with contradictory constraints, which is the case for a variable-camber morphing wing in which flexibility, stiffness and weight of the structure all need to be considered simultaneously.

To be able to perform a topology optimization of shape-morphing structures, several modelling assumptions were made. These assumptions are presented below. For the topology optimization, a density-based approach with a structured mesh is used. This means that the design domain of the optimization is meshed using rectangular finite elements. The design domain refers to the area of the domain where the densities of the elements are the variables of the optimization. A structured mesh with rectangular elements was chosen, because of the relatively low computational effort this implies. This is due to the fact that the stiffness matrix for each element is the same and as such calculating one stiffness matrix suffices, instead of having to individually calculate all matrices for all elements. To find the individual stiffness matrix of an element, it only needs to be multiplied by the Young's modulus of that element. How this Young's modulus is determined is discussed in Section 2.2. In the structured mesh-type, all elements are the same rectangular shape. Therefore, this type of meshing is generally only applicable to rectangular design domains. All structures in this thesis are modelled in 2D, since a 3D model would be much more extensive and involve more computational effort. The goal here is to see if the density-based topology optimization yields a satisfactory result in 2D before extending to 3D simulations. Non-linearities of the structures will not be taken into account. A linear analysis will be used, since this is less computationally intensive. The focus is on small displacements and rotations for which it is assumed that a linear analysis will give a sufficient approximation.

The rest of this Chapter will focus on the steps that are necessary, within each design iteration

of the topology optimization process, to extract the displacement field of the obtained structure for the current values of the design variables so this can be used for the objective function and thus to evaluate the performance of the structure.

## 2.2 Analysis of the obtained structure within each iteration

A gradient based optimizer, MMA, will be used to update the values of the design variables for each iteration in the optimization. This is done based on current values and sensitivities of the objective and constraint functions. To evaluate the objective and constraint functions, several steps are incorporated in every iteration to obtain the displacement field of the structure resulting from the current values of the design variables. This Section will discuss these steps in detail. The full process is visualized in Fig. 2.1. The vector  $\mathbf{x}$  represents a density distribution over the design domain. These densities are the design variables of the problem.

The first step is to filter this density distribution. Filtering is necessary to avoid checkerboarding and mesh-dependency [17]. The filter will define a filtered density  $\tilde{\mathbf{x}}$  as a weighted average of the design variables in a neighbourhood of radius  $r_{\text{fil}}$ . The filtered variables  $\tilde{\mathbf{x}}$  will look like [29]:

$$\tilde{\mathbf{x}} = \mathbf{D}_I \mathbf{x} \quad (2.1)$$

In this equation, the matrix  $\mathbf{D}_I$  is a matrix that includes the weights and constant parameters associated with the filter. For more background on how this matrix is set-up, refer to Fernández, Yang, Koppen, *et al.* [29].

To further improve on the manufacturability of the design, a robust design approach is adopted that adds eroded, dilated and intermediate density distributions [30]. The eroded distribution ( $\tilde{\mathbf{x}}^{\text{ero}}$ ) represents a uniformly thinned structure, the dilated distribution ( $\tilde{\mathbf{x}}^{\text{dil}}$ ) represents a uniformly thickened structure and the intermediate distribution ( $\tilde{\mathbf{x}}^{\text{int}}$ ) represents the intended design. These three designs are obtained from the filtered density field using the following smoothed Heaviside function [29]:

$$\tilde{x}_e = H(\tilde{x}_e, \beta, \mu) = \frac{\tanh(\beta\mu) + \tanh(\beta(\tilde{x}_e - \mu))}{\tanh(\beta\mu) + \tanh(\beta(1 - \mu))}. \quad (2.2)$$

In this equation,  $\tilde{x}_e$  represents the filtered variable. The parameter  $\beta$  controls the steepness of the Heaviside function and decreases the number of grey elements in the design. The parameter  $\mu$  controls the threshold of the projection. The eroded, dilated and intermediate designs are obtained for the same  $\beta$  while  $\mu$  is varied. The Heaviside projection is implemented in such a way that over the course of the iterations  $\beta$  is exponentially increased until a specified final value is reached. This way, the optimization is forced towards a 0-1 configuration, meaning that elements either have density 0 or density 1. To keep this section brief, from here on out the process will be described using only variables  $\tilde{\mathbf{x}}$ . The three designs will not be further used in the equations. For the objective and constraint functions it will be clarified in the text which design (i.e. dilated, eroded or intermediate) is involved as well as in the final optimization formulation.

After the projection the Young's modulus of the elements is determined by the modified simplified isotropic material with penalization (SIMP) approach [31]:

$$\hat{x}_e = x_{\min} + \tilde{x}_e^p (1 - x_{\min}). \quad (2.3)$$

In this formulation,  $x_{\min}$  is the minimal density that can be prescribed to an element, which is defined as  $x_{\min} = E_{\text{void}}/E$ . Here,  $E_{\text{void}}$  signifies the Young's modulus that is prescribed to a void element and  $E$  is the Young's modulus of the material.  $p$  is the penalty factor (usually set to 3) and  $x_{\min}$  is usually set to a small positive number, to avoid singularity of the stiffness matrix. The density variables  $\hat{x}_e$  are linearly translated to the Young's modulus by:  $E_e = \hat{x}_e E$ .

In the next steps, the system stiffness matrix  $\mathbf{K}$  is assembled and the following finite element problem is solved:

$$\mathbf{K} \mathbf{u} = \mathbf{p}. \quad (2.4)$$

In this equation,  $\mathbf{u}$  indicates the nodal displacement field of the structure and  $\mathbf{p}$  indicates the external nodal loads. The obtained nodal displacement field can then be used to evaluate the performance of the structure in this iteration. More on this performance evaluation can be found in Chapter 3.

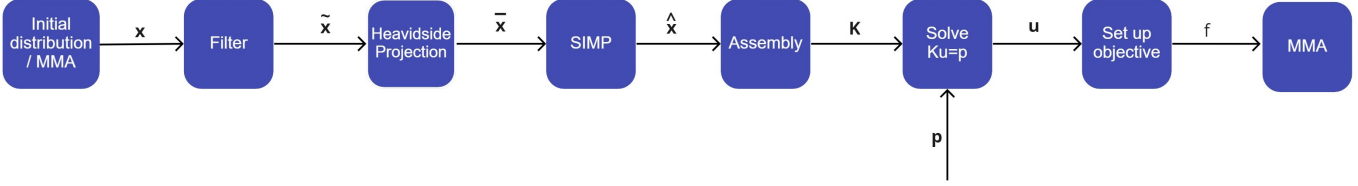


Figure 2.1: A graphical representation of the analysis in each iteration of the topology optimization process

## 2.3 Sensitivities

To enable the optimizer to improve the functionality of the design, sensitivity information is required. These sensitivities are used by the gradient based optimizer to update the design variables. Please note that in this section, for the purpose of clarity and brevity, the dependencies of each function are not written down explicitly. The sensitivities of the responses, that is the objective function and constraints, need to be evaluated with respect to the design variables. In order to do that, the sensitivity of the output of each block in the flowchart of Fig. 2.1 with respect to the input of that block needs to be calculated. Using the chainrule, the final sensitivity of a function can then be found. The sensitivity of the objective function ( $f$ ) can be calculated as:

$$\frac{df}{dx} = \frac{df}{du} \frac{du}{d\mathbf{K}} \frac{d\mathbf{K}}{d\hat{\mathbf{x}}} \frac{d\hat{\mathbf{x}}}{d\bar{\mathbf{x}}} \frac{d\bar{\mathbf{x}}}{d\tilde{\mathbf{x}}} \frac{d\tilde{\mathbf{x}}}{d\mathbf{x}}. \quad (2.5)$$

In the first step, the sensitivities of the density filter and Heaviside projection can be calculated as [29]:

$$\frac{d\bar{\mathbf{x}}}{d\mathbf{x}} = \frac{d\bar{\mathbf{x}}}{d\tilde{\mathbf{x}}} \frac{d\tilde{\mathbf{x}}}{d\mathbf{x}} = \mathbf{D}_f \mathbf{J}. \quad (2.6)$$

Here  $\mathbf{J}$  is the Jacobian of the Heaviside function defined as  $\mathbf{J} = \text{diag}(H'(\tilde{x}_1), \dots, H'(\tilde{x}_N))$ . Here  $H'(\tilde{x}_i)$  is the derivative of  $H$  with respect to  $\tilde{x}_i$ . The sensitivity of the SIMP interpolation is fairly straightforward:

$$\frac{\partial \hat{\mathbf{x}}}{\partial \tilde{x}_e} = p \tilde{x}_e^{p-1} (1 - x_{\min}). \quad (2.7)$$

The sensitivities  $\frac{d\mathbf{u}}{d\mathbf{K}} \frac{d\mathbf{K}}{d\hat{\mathbf{x}}}$  can be directly calculated as  $\frac{d\mathbf{u}}{d\hat{\mathbf{x}}}$ , via differentiation of  $\mathbf{K}\mathbf{u} = \mathbf{p}$ :

$$\frac{d\mathbf{K}}{d\hat{\mathbf{x}}} \mathbf{u} + \mathbf{K} \frac{d\mathbf{u}}{d\hat{\mathbf{x}}} = \frac{d\mathbf{p}}{d\hat{\mathbf{x}}}. \quad (2.8)$$

Which yields:

$$\frac{d\mathbf{u}}{d\hat{\mathbf{x}}} = \mathbf{K}^{-1} \left( \frac{d\mathbf{p}}{d\hat{\mathbf{x}}} - \frac{d\mathbf{K}}{d\hat{\mathbf{x}}} \mathbf{u} \right). \quad (2.9)$$

Where  $\frac{d\mathbf{p}}{d\hat{\mathbf{x}}} = 0$ . However,  $\frac{d\mathbf{u}}{d\hat{\mathbf{x}}}$  is usually not directly calculated because of the computational effort this involves. Instead, the adjoint method is used, which results in the following sensitivity for the objective function:

$$\frac{df}{d\mathbf{x}} = -\lambda^T \frac{d\mathbf{K}}{d\hat{\mathbf{x}}} \mathbf{u} \frac{d\hat{\mathbf{x}}}{d\mathbf{x}} \quad (2.10)$$

Where  $\lambda$  can be found from solving the adjoint equation:

$$\mathbf{K}\lambda = \frac{df}{d\mathbf{u}} \quad (2.11)$$

For more information on this, please refer to Tortorelli and Michaleris [32].

To complete the sensitivity analysis, the sensitivities of the objective function  $f$  and constraint functions  $g_k$  should be evaluated. These are set-up for the compliant variable-camber morphing wing design problem in Chapter 4.



## Chapter 3

# Objective function investigation

In this Chapter, an investigation into an objective function that can evaluate the shape of a shape-morphing structure is presented. First, the least-squares-error (LSE) objective function that is often suggested in the literature for this application is discussed in Section 3.1. This is done based on a numerical example involving a shape-adaptable surface mechanism. In Section 3.2, the performance of the LSE objective function in the more complex case is compared to the performance of a dot-product objective and in Section 3.3, an optimization of the stiffnesses of several springs in series is performed in order to explain the difference between performance of the two objective function formulations.

### 3.1 Shape-adaptable surface mechanisms with a LSE objective function

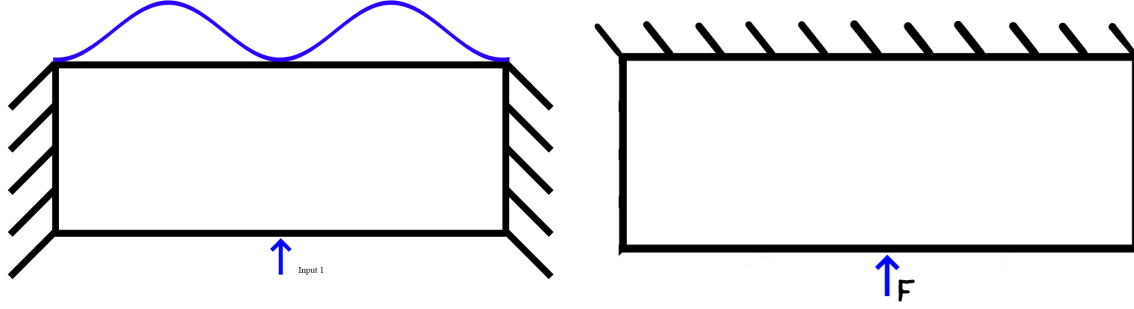
In the literature, a least squares error (LSE) is frequently suggested as an objective function for the optimization of compliant shape-morphing structures, look for example at Lu and Kota [22] and Tong, Ge, Sun, *et al.* [25]. A typical LSE objective is defined as:

$$\text{LSE} = \sqrt{\sum_{i=1}^N (x_i^{\text{def}} - x_i^{\text{tar}})^2 + \sum_{i=1}^N (y_i^{\text{def}} - y_i^{\text{tar}})^2}. \quad (3.1)$$

In this equation,  $x^{\text{def}}$  and  $y^{\text{def}}$  define the coordinates of several sample points on the surface in the deformed state.  $x^{\text{tar}}$  and  $y^{\text{tar}}$  are the coordinates of these same sample points in the desired deformed shape. This way, the position of the sample points in the deformed state here obtained from the finite element analysis in the iteration, can be compared to their desired position and be improved upon by the optimization.

To test the effectiveness of this objective, a test case was set up for a compliant shape-adaptable surface mechanism. This is a mechanism which should change the shape of its top surface as a response to a prescribed input displacement. Two different loading conditions were considered in this optimization. First of all, see Fig. 3.1a. The goal of the optimization is to obtain a compliant mechanism that can deform the top surface into a cosine shape, as defined by the blue line, for a prescribed unit input displacement at input 1. The top surface of the mechanism is a non-design domain with element densities  $x_e = 1$ , and both sides are fixed. When elements are part of the non-design domain, the elements densities  $x_e$  are fixed and are not part of the variables of the optimization. This loading case is clarified in further equations by subscript 1. The second load case (see Fig. 3.1b) is used in the optimization to impose a compliance constraint that will ensure a certain amount of stiffness between the input and output. For this constraint, the compliance of the structure ( $C(\mathbf{x})$ ) should be smaller than a certain amount  $C_{\text{max}}$ . The compliance of the structure is imposed on the eroded design and can be calculated by:

$$C(\mathbf{x}) = \mathbf{u}(\mathbf{x})^T \mathbf{K}(\mathbf{x}) \mathbf{u}(\mathbf{x}) = \mathbf{u}(\mathbf{x})^T \mathbf{p}. \quad (3.2)$$



(a) boundary conditions, design domain and objective for the shape adaptable complaint mechanism. A mechanism should be obtained of which the top surface gains the shape described by the blue line, for an input displacement at input 1

(b) The boundary conditions for the loadcase for which a compliance constraint was implemented. For input for F, there should be a maximal amount of compliance.

Figure 3.1: The two loadcases for the optimization of the shape-adaptable surface mechanism. a) shows the loadcase for which the system is optimized, b) shows the loadcase for which the compliance constraint was implemented.

Since  $\mathbf{p}$  is the prescribed load on the input, this basically places a constraint on the displacement of the node at which the force is applied. This constraint is imposed on the load condition as shown in Fig. 3.1b, this load case will be clarified in equations with the subscript 2.

A volume constraint, which restricts the total amount of volume of the obtained structure, was also imposed. This is done by placing a constraint on the volume of the structure, in which the volume may not exceed a specified maximum volume. This is included in the optimization by placing a constraint on the mean volume fraction of the design domain as follows:

$$\frac{\sum_{e=1}^N x_e}{N} \leq V_{\max}. \quad (3.3)$$

In this equation,  $V_{\max}$  represents the maximum mean volume fraction of the design domain and  $N$  is the total number of design variables.

The optimization problem in negative-null form then is defined as:

$$\begin{aligned} \min \quad & f(\mathbf{x}) = \sqrt{\sum_{i=1}^M (u_{1,i}^{\text{def,int}} - u_i^{\text{tar}})^2}, \\ \text{s.t.} \quad & \frac{\mathbf{u}_2(\mathbf{x}^{\text{ero}})^T \mathbf{p}}{C_{\max}} - 1 \leq 0, \\ & \frac{\sum_{e=1}^N x_e}{NV_{\max}} - 1 \leq 0, \\ & 0 \leq x_{\min} \leq x_e \leq 1, \quad e = 1, \dots, N. \end{aligned} \quad (3.4)$$

Where  $M$  is the total amount of nodes on the top surface,  $u_{1,i}^{\text{def}}$  is the obtained nodal displacement in vertical direction for node  $i$  on the top surface as predicted by the finite element analysis for the first load case and  $u_i^{\text{tar}}$  is the target nodal displacement of node  $i$ .

The values chosen for the several constants in the optimization can be found in Table 3.1. The material constants were assumed to be Young's modulus  $E = 69$  GPa, Poissons ratio  $\nu = 0.32$  and density  $\rho = 2710$  kg/m<sup>3</sup>. The compliance constraint was implied for the second load case. The goal here is to ensure that a maximum amount of displacement of  $1e - 5$  m of this node is obtained if the force is set to  $F = 1$  N. The maximum volume fraction  $V_{\max}$  was set to 0.4.

The obtained structure for this problem is shown in Fig. 3.2a. These are the scaled results of the linear analysis, this will be true for all deformed structures shown in this Chapter. As can be seen in Fig. 3.2b, the output shape of the top surface is indeed a cosine, which indicates that the LSE objective function performs well here.

Table 3.1: Constant values for the topology optimization of the shape-adaptable surface mechanism

Constant	Value
$E$	69e9 GPa
$\nu$	0.32
$\rho$	2710 kg/m <sup>3</sup>
$F$	1 N
$C_{\max}$	1e - 5
$V_{\max}$	0.4
$\beta$	0.5
$\mu$	0.5

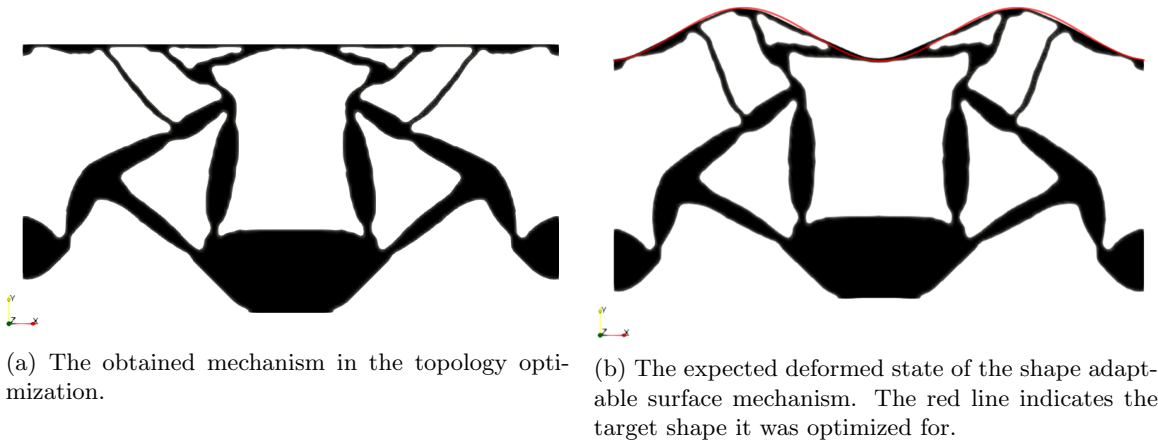


Figure 3.2: The obtained shape adaptable surface mechanism in both undeformed (a) and deformed (b) state

Next, the LSE was tested for a more complex case in which a second input was added for which the top surface should obtain a different shape than for input 1. This was done to see if the LSE objective is also able to obtain good results for complex cases relevant to the compliant variable-camber morphing wing design. The location of the second inputs and the shapes are defined in Fig. 3.3. The first input should now obtain a cosine of double the wavelength than before, while inputs 2 (which are simultaneously actuated) should obtain the original cosine shape. When input 1 is actuated, inputs 2 are fixed and vice versa. The boundary conditions and compliance load case do not change. The obtained mechanism in this case can be seen in Fig. 3.4, and the deformed shapes in Fig. 3.5.

As can be seen, the deformed shapes for the more complex case are not very satisfactory. For input 1, the top surface does not resemble the preferred output shape at all. Inputs 2 do slightly better as the output shape is recognizable, but still very different from the prescribed shape.

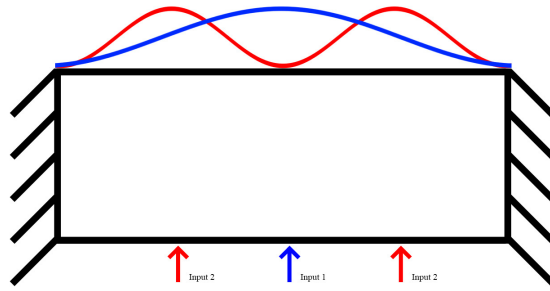
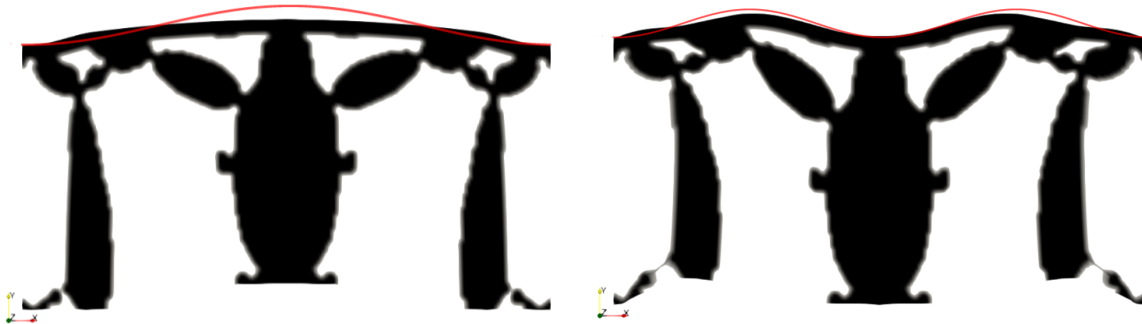


Figure 3.3: The second, more complex situation for the shape adaptable compliant mechanism. The two different input displacements should produce a different shape of the top surface. A displacement at input 1 should produce the blue target curve. Input displacements at inputs 2 should produce the red target curve.



Figure 3.4: The shape adaptable mechanism obtained for 2 different inputs and outputs for the LSE objective function, as defined in Fig. 3.3



(a) The deformed state of the shape-adaptable surface mechanism with the LSE objective function when input 1 is actuated. The red line indicates the desired deformed shape of the top surface.

(b) The deformed state of the shape-adaptable surface mechanism with the LSE objective function when inputs 2 are actuated. The red line indicates the desired deformed shape of the top surface.

Figure 3.5: The deformed states of the shape-adaptable surface mechanisms for the two different inputs obtained from the optimization with a LSE objective function. in (a) input 1 is active, while in (b) inputs 2 are active.

### 3.2 Comparison LSE and dot-product objective function for a shape-adaptable surface mechanism

To improve on the performance of the topology optimization, a different type of objective function was proposed and implemented for the shape-adaptable surface mechanism. The objective function  $f(\mathbf{x})$  is developed using a dot-product, where the magnitudes of the displacement vectors are divided out. This formulation is defined as:

$$f(\mathbf{x}) = 1 - \frac{\mathbf{u}^{\text{tar}} \cdot \mathbf{u}^{\text{def}}(\mathbf{x})}{|\mathbf{u}^{\text{tar}}| |\mathbf{u}^{\text{def}}(\mathbf{x})|}. \quad (3.5)$$

Where  $0 \leq f(\mathbf{x}) \leq 1$ . This objective purely focuses on the shape of the deformed surface, while the magnitude of the total deformation is not taken into account. The minimal magnitude of the deformation will be specified by a constraint. Since the deformed state is not completely fixed, there is some freedom in the output displacement magnitude. The optimization then becomes:

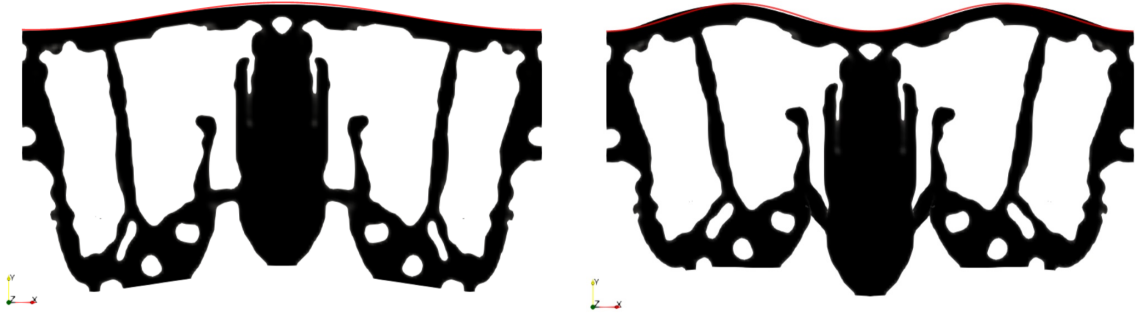
$$\begin{aligned} \min \quad & f(\mathbf{x}) = 1 - \frac{\mathbf{u}^{\text{tar}} \cdot \mathbf{u}_1^{\text{def}}(\mathbf{x}^{\text{int}})}{|\mathbf{u}^{\text{tar}}| |\mathbf{u}_1^{\text{def}}(\mathbf{x}^{\text{int}})|}, \\ \text{s.t.} \quad & -\frac{u_{\text{maxinp1},1}^{\text{int}}}{u_{\text{min}}} + 1 \leq 0, \\ & -\frac{u_{\text{maxinp2},1}^{\text{int}}}{u_{\text{min}}} + 1 \leq 0, \\ & \frac{\mathbf{u}_2(\mathbf{x}^{\text{ero}})^T \mathbf{p}}{C_{\text{max}}} - 1 \leq 0, \\ & \frac{\sum_{e=1}^N x_e}{NV_{\text{max}}} - 1 \leq 0, \\ & 0 \leq x_{\text{min}} \leq x_e \leq 1, \quad e = 1, \dots, N. \end{aligned} \quad (3.6)$$

Here,  $u_{\text{maxinp1},1}$  indicates the displacement of the node at the top of the prescribed cosine shape for input 1 and  $u_{\text{maxinp2},1}$  indicates the displacement of the node at the top of the prescribed cosine shape for inputs 2. For the obtained structure see Fig. 3.6 and for the deformed shapes see Fig. 3.7. As can be seen in these figures, the dot-product objective obtained much better results than the LSE objective as the shapes for both input 1 and inputs 2 match the prescribed shapes nearly perfectly.

The question now remains why is this dot-product objective more effective than the LSE objective. One of the reasons might be that the LSE is very restrictive as there is not only a specific shape prescribed, but also an exact displacement of all sample points is required. The dot-product has a bit more freedom here, since the exact displacements are filtered out. The goal of the objective is to gain a certain shape, where a minimum amount of output displacement is prescribed in a constraint. This displacement is not entirely fixed, but has only a lower bound. This means that, even if the displacement is a bit bigger, while the output shape remains similar to the prescribed shape, the objective still goes towards zero. This way, the dot product has multiple optimums while the LSE objective has strictly one minimum. This should make it easier for the optimizer to find a minimum in the dot-product case. To gain understanding of how these two different types of objective functions behave, a minimum working example with two variables was analysed. The results of this can be found in Section 3.3.



Figure 3.6: The shape adaptable mechanism obtained for 2 different inputs and outputs as defined in Fig. 3.3, for the dot product objective



(a) The deformed state of the shape-adaptable surface mechanism when input 1 is actuated, for the dot-product objective. The red line indicates the desired deformed shape of the top surface.

(b) The deformed state of the shape-adaptable surface mechanism when inputs 2 are actuated, for the dot-product objective. The red line indicates the desired deformed shape of the top surface.

Figure 3.7: The deformed states of the shape-adaptable surface mechanisms for the two different inputs, with a dot product objective. in (a) input 1 is active, while in (b) inputs 2 are active.

### 3.3 A minimum working example

To analyze the behaviour of the two different objective functions an example was set up using two springs in series, see Fig. 3.8. For the first optimization, the stiffnesses  $k_1$  and  $k_2$  are the design variables. This problem is optimized for a target displacement  $u^{\text{tar}}$  of the two nodes, while the system is subjected to force  $F$ . This optimization is performed using `fmincon` in Matlab [33], with a sequential quadratic programming (SQP) algorithm. This is gradient based, in which the sensitivities are calculated using finite differences. The code for this optimization can be found in Appendix A.0.1. The following optimizations were performed:

$$\begin{aligned}
 \min \quad & f(\mathbf{k}) = 1 - \frac{\mathbf{u}^{\text{tar}} \cdot \mathbf{u}^{\text{def}}(\mathbf{k})}{|\mathbf{u}^{\text{tar}}| |\mathbf{u}^{\text{def}}(\mathbf{k})|}, \\
 \text{s.t.} \quad & \frac{u_2}{u_2^{\text{tar}}} - 1 = 0, \\
 & k_i > 0 \quad i = 1, 2,
 \end{aligned} \tag{3.7}$$

$$\begin{aligned}
 \min \quad & f(\mathbf{k}) = \sqrt{\sum_{i=1}^2 (u_i^{\text{def}} - u_i^{\text{tar}})^2}, \\
 \text{s.t.} \quad & k_i > 0 \quad i = 1, 2.
 \end{aligned} \tag{3.8}$$

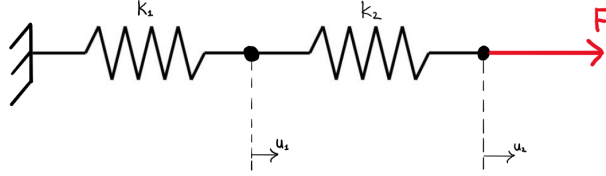
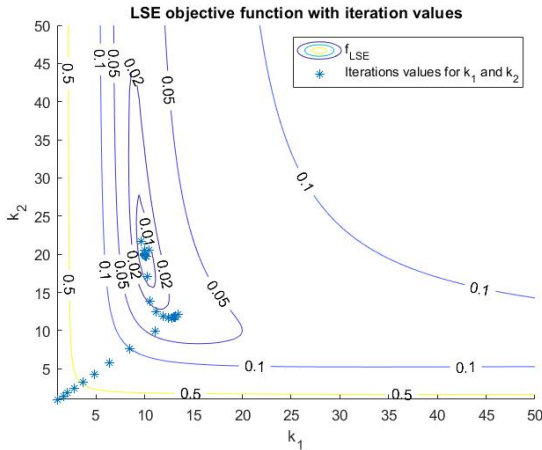
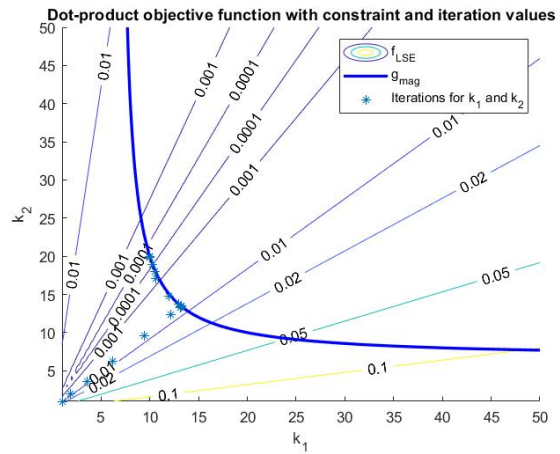


Figure 3.8: The example used to analyse the behaviour of the two different objective functions. Two linear springs in series, with a force  $F$  applied in horizontal direction to the second node.

The constraint on the output displacement for the dot-product objective (Eq. (3.7)) is here placed as an equality constraint, to make sure both cases iterate towards the same optimum. This will allow for a comparison of their convergence speed and performance. For this optimization,  $\mathbf{u}^{\text{tar}} = [0.1 \ 0.15]$ , with initial values for  $\mathbf{k} = [1 \ 1]$ . The results are displayed in Fig. 3.9. The contour plots of the objective functions show a clear difference between the shapes of the two objectives. While the LSE objective has one clear optimum located in a slender valley, the dot-product objective has a complete line of optima and the optimum is constrained by the equality constraint. This equality constraint has the same shape as the valley of the LSE objective (see Fig. 3.9b). Both formulations resulted in the (correct) optimum of  $\mathbf{k} = [10 \ 20]$ . The dot-product formulation obtained this optimum in 19 iterations, and the LSE formulation obtained it in 44 iterations. The dot-product thus finds the optimum more than twice as fast as the LSE formulation. Please note that different values for the target displacement and initial design were tried, but all yielded similar results.



(a) In this figure, a contour plot of the LSE objective function for the spring example is shown. The stars indicate the values of  $k_1$  and  $k_2$  for the different iterations in the optimization process.



(b) In this figure, a contour plot of the dot-product objective function for the spring example is displayed. The blue line is the equality constraint on the magnitude of the output displacement (as defined in Eq. (3.7)). The stars indicate the values of  $k_1$  and  $k_2$  for the different iterations in the optimization process.

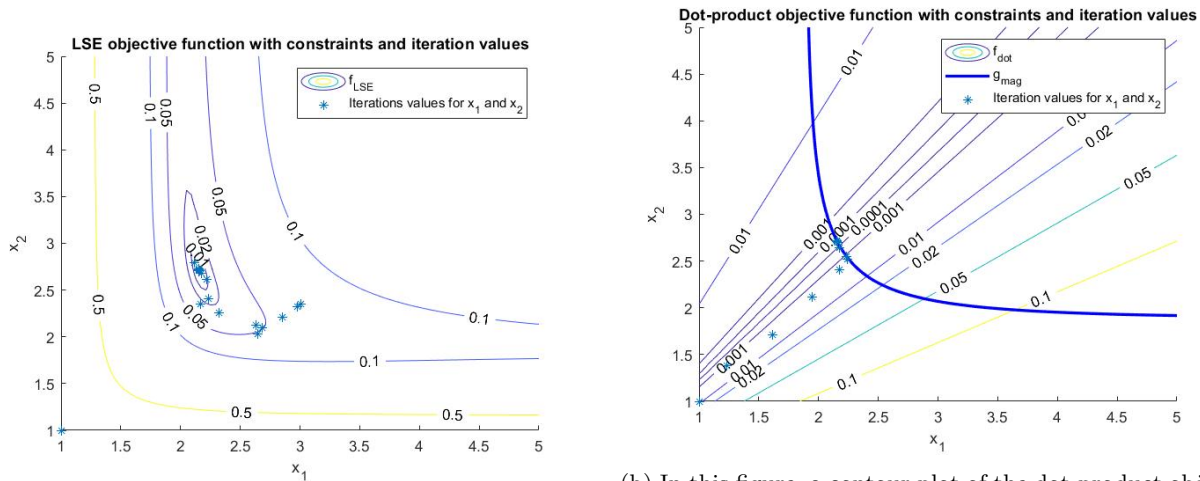
Figure 3.9: Contour plots of the two different objective functions including constraints and iterations for an optimization of the stiffnesses of two springs in series. in a) the plot for the LSE objective function, in b) the plot of the dot-product objective function

To make the example more equivalent to the topology optimization, the spring stiffnesses were assumed to be depended on density  $\mathbf{x}$ , where  $k_i = x_i^3$ . The results of this can be found in Fig. 3.10 (for the Matlab script, see Appendix A.0.2). For this example the difference in number of iterations is even more profound. While the LSE formulation needs 29 iterations in order to find the optimum, the dot-product formulation only needs 11. These results all seem to indicate that the dot-product formulation creates an objective function which is easier to minimize, than the LSE formulation. While the dot-product has a line at which it becomes zero and always one clear direction in which to move in order to decrease the value of the objective value, the optimum of the LSE is located in a slender valley. The shape of this valley seems to be what causes the difficulty in finding the optimum for the LSE case. Once the objective function value for an iteration is located in the valley, it can be seen that many, small steps in variable value are needed before the optimizer reaches the optimum (see Fig. 3.11).

Finally, the optimization was extended to include more springs in series, to asses how this influences the results of the different objectives (for the Matlab script, see Appendix A.0.3). For this  $\mathbf{u}^{\text{tar}}$  was quadratically increased for each point according to:

$$u_i^{\text{tar}} = 0.05(i - 1)^2 + 0.1 \quad (3.9)$$

Where  $i$  is the number of springs in the optimization. The results are displayed in Table 3.2. It can be seen that if the number of springs, and therefore the number of variables, is increased the LSE formulation consistently requires more iterations to reach the optimum than the dot-product formulation does. In the lower regions ( $N = 2, 3, 4, 10, 50, 100$ , with  $N$  signifying the number of springs and thus the number of design variables) the ratio between number of iterations for the LSE-objective and the dot-product objective stays between 0.9 and 3. However, when the complexity of the optimization is increased by increasing the number of design variables up to 500, the difference in performance becomes much more pronounced. The optimization with the dot-product objective gets to the optimum up to 15 times faster than the LSE optimization. The dip in the ratio for 50 variables is a coincidence, when the optimization is run with slightly different starting conditions, the number of iterations for the LSE immediately jumps up to 377, while the amount of iterations for the dot-product stays roughly the same at 271. These results are a clear indication that the dot-product



(a) In this figure, a contour plot of the LSE objective function for the spring example is shown, where  $k_i = x_i^3$ . The stars indicate the values of  $x_1$  and  $x_2$  for the different iterations in the optimization process

(b) In this figure, a contour plot of the dot-product objective function for the spring example is displayed, where  $k_i = x_i^3$ . The blue line is the equality constraint on the magnitude of the output displacement (as defined in Eq. (3.7)). The stars indicate the values of  $x_1$  and  $x_2$  for the different iterations in the optimization process

Figure 3.10: Contour plots of the two different objective functions including constraints and iterations for an optimization of the stiffness of two springs in series. In a) the plot for the LSE objective function, in b) the plot for the dot-product objective function.

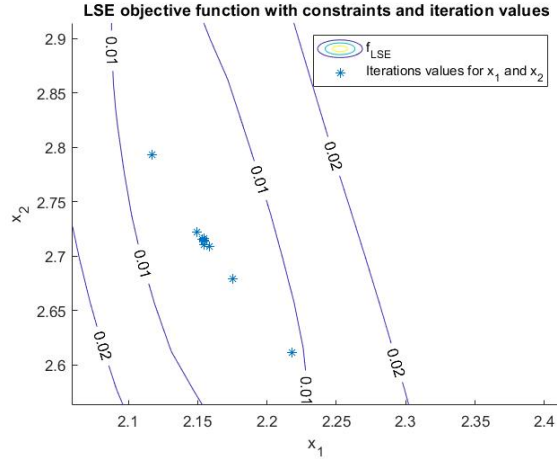


Figure 3.11: A zoom of the valley of the LSE objective function from Fig. 3.10a. It can be seen that in the valley many iterations are needed, with very small steps, in order to find the optimum of the objective function

objective performs better than the LSE objective. While for simple cases this difference is only noted in the amount of iterations needed to find the optimum, it is hypothesized that once the optimization becomes more complex, including more constraints, this could result in the LSE optimization not reaching an optimum, while the dot-product still does. This can explain why the dot-product objective produces better results in complex topology optimizations than the LSE objective function does.

It can be concluded from the above that for the density-based topology optimization of compliant shape-morphing structures the dot-product objective function is the best option. It converges faster than its LSE counterpart and is more capable to reach an optimum in complex cases.

Table 3.2: This table contains the number of iterations needed for the different objective function formulations, with a different amount of springs in series. Each spring equals one design variables, so the amount of springs is equal to the number of design variables in the optimization.

Number of springs	Number of iterations LSE	Number of iterations dot-product	Ratio LSE:dot-product
3	44	15	2.9333
4	43	22	1.9545
10	88	74	1.1892
50	266	284	0.9366
100	414	242	1.7107
500	1959	130	15.0692



# Chapter 4

## Numerical examples

In this Chapter, the suggested method for the topology optimization of shape-morphing structures will be applied to the design of a compliant variable-camber morphing wing in two numerical examples. In Section 4.1, the problem definition of the variable-camber morphing wing will be discussed, the final optimization formulation including the objective function and constraint functions and their sensitivities will be discussed and the constants used during the topology optimization will be presented. In Section 4.2, a numerical example is presented, in which a problem arose with the value of  $x_{\min}$ . Finally in Section 4.3, the final design of the variable-camber morphing wing will be presented and analysed.

### 4.1 The design problem of a variable-camber morphing wing

In this Section, the design problem of a variable-camber morphing wing will be further defined. In Section 4.1.1, the problem is defined, and in Section 4.1.2 the optimization formulation is presented, including the sensitivities of the objective and constraint functions.

#### 4.1.1 Problem definition of a variable-camber morphing wing

The morphing trailing edge will be designed using the NACA 2412 airfoil shape with a chord length of 200 mm, which is suitable for an unmanned, small aircraft. Since the focus is on the trailing edge, only the second half of the profile is considered. In the optimization, two different loading conditions are taken into account. First, there is the loading condition where the actuator provides an input force (see Fig. 4.1a). Here it is assumed that the top left side of the skin is where the morphing trailing edge is rigidly attached to the front part of the airfoil profile. The actuation of the trailing edge is located at the bottom left. This is a slider system which is why this part of the wing is constraint in vertical direction. The actuator provides an input force in horizontal direction. The second loading condition, as presented in Fig. 4.1b, is the case where the dynamic pressure on the wing is modelled. In order to have a representation of dynamic pressure on the surface of the wing that the trailing edge should be able to endure, it is calculated based on a fixed airspeed of  $v = 20$  m/s. This airspeed is equivalent to airspeeds for small, unmanned aircrafts [34]. The pressure on the airfoil can then be calculated via [35]:

$$q = \frac{1}{2} \rho v^2. \quad (4.1)$$

In this equation,  $q$  represents the dynamic pressure on the wing and  $\rho = 1.225$  kg/m<sup>3</sup> represents the density of air. This results in a dynamic pressure of 245 Pa. In reality, the pressure profile differs over the airfoil, however for simplicity it is here assumed that the pressure is equally distributed over the airfoil surface.

The desired deformed shape of the airfoil is a quadratic shape with constant curvature. It has been shown that such a parabolic flap has good aerodynamic performance as it can increase the lift coefficient with a low drag penalty [2], [7], [36]–[38]. The desired deformed shape can be seen in Fig. 4.2. It should be noted that for the purpose of the topology optimization only the shape of the top surface is considered in the objective

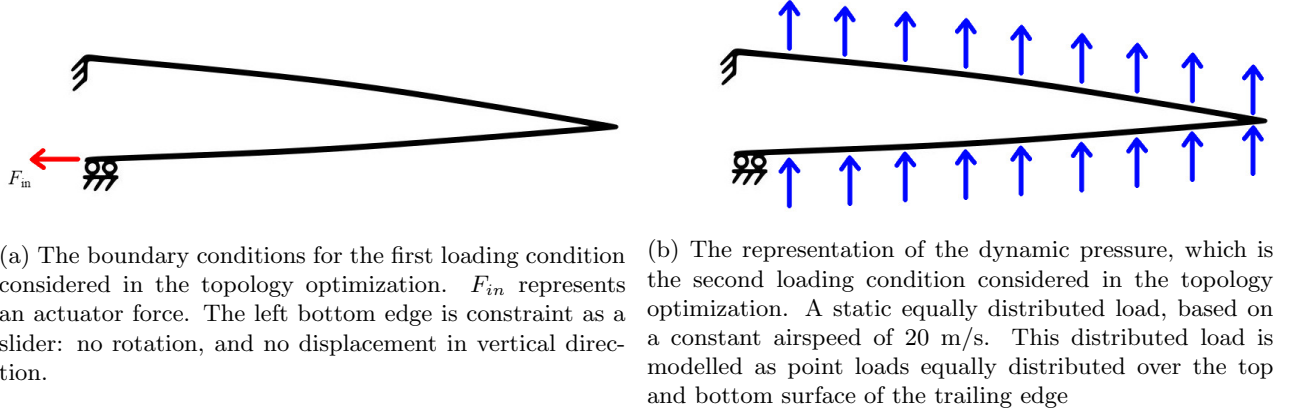


Figure 4.1: Schematics of the boundary conditions (a) and the representation of the dynamic pressure (b).

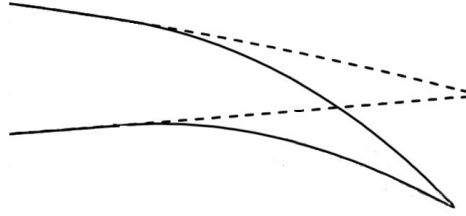


Figure 4.2: A graphical representation of the desired shape of the morphing trailing edge. The dashed line indicates the original, neutral shape of the airfoil, the solid line represents the desired deformed shape of the airfoil. Adapted from [38]

function. The topology optimization is therefore concerned with creating a structure with a top surface that has a quadratic shape after deformation, i.e. the top surface should follow a curve defined by  $y = -ax^2$ , where  $y$  is the vertical displacement of a node on the top surface at location  $x$ . The  $a$  is a constant.

As was mentioned in the previous Chapter, a structured mesh with rectangular elements is used to mesh the design domain. This is usually applicable to rectangular design domains. However, the design domain of the NACA 2412 airfoil is not rectangular. To circumvent this problem, the shape of the airfoil can be projected onto the rectangular mesh, see Fig. 4.3. The elements outside the airfoil are then selected as a non-design domain, comprising of void elements. The elements on the edge of the domain, i.e. the skin of the morphing wing, are also designated non-design domains, but are assigned as containing material ( $x_e = 1$ ). This is graphically represented in Fig. 4.3.

### 4.1.2 Optimization formulation

The optimal final configuration for the top surface of the variable-camber morphing wing is the quadratic shape which is defined by  $\mathbf{u}^{\text{tar}}$ .  $\mathbf{u}^{\text{tar}}$  is a displacement vector that contains the target displacements in vertical direction of the nodes on the top surface of the trailing edge. This displacement field needs to be compared with the displacement field of those degrees of freedom obtained from the finite element analysis in the current iteration of the optimization. The relevant degrees of freedom, that is to say the vertical degrees of freedom of the nodes on the top surface of the trailing edge, are selected from  $\mathbf{u}(\mathbf{x})$  and stored in vector  $\mathbf{u}_{\text{top}}(\mathbf{x})$ . This is done via:

$$\mathbf{u}_{\text{top}} = \mathbf{L}\mathbf{u} \quad (4.2)$$

In this equation,  $\mathbf{L}$  is a selection vector which selects the vertical displacements of the nodes on the top surface of the trailing edge.

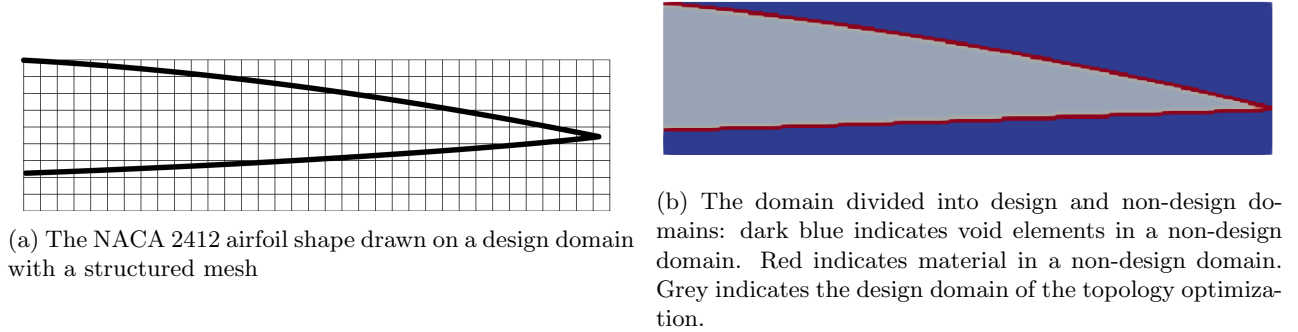


Figure 4.3: The build-up of the design and non-design domains of the optimization. in a) the shape of the NACA 2412 airfoil drawn on the structured mesh. in b) the build up of the design and non-design domains is shown.

Please note that  $\mathbf{u}$  implicitly depends on  $\mathbf{K}$  and  $\mathbf{K}$  is dependent on  $\hat{\mathbf{x}}$  and so on. However, for ease of notation we will here write a direct dependency on  $\mathbf{x}$ . These vectors are then used in the dot-product objective function as described in the previous Chapter.

The constraints of the optimization revolve around the three main requirements of the morphing wing namely flexibility, stiffness and weight. First, a constraint is placed on the magnitude of the output displacement. This constraint ensures that the structure is flexible enough to obtain a certain amount of output displacement for a specified actuator input force. This constraint is formulated as a minimal amount of displacement ( $u_{\min}$ ) for the tip of the trailing edge ( $u_{\text{tip}}(\mathbf{x})$ ). It is placed on the dilated design, since this is the most stiff design and for the loadcase as represented in Fig. 4.1a. Second, a compliance constraint was integrated for the dynamic pressure as presented in Fig. 4.1b in which the compliance of the structure ( $C(\mathbf{x})$ ) should be smaller than a certain amount  $C_{\max}$ . This ensures that the shape of the trailing edge does not change while it is subjected to dynamic pressure during flight.

Finally, to ensure a light-weight structure, a constraint should be placed on the maximum allowed mass of the structure. This is done by placing a constraint on the volume of the structure, in which the volume may not exceed a specified maximum volume. This is included in the optimization by placing a constraint on the mean volume fraction. The topology optimization of the compliant trailing edge can then be expressed in negative null-form as:

$$\begin{aligned}
\min \quad & f(\mathbf{x}) = 1 - \frac{\mathbf{u}^{\text{tar}} \cdot \mathbf{u}_{\text{top},1}^{\text{int}}(\mathbf{x})}{|\mathbf{u}^{\text{tar}}| |\mathbf{u}_{\text{top},1}^{\text{int}}(\mathbf{x})|}, \\
\text{s.t.} \quad & -\frac{u_{\text{tip},1}^{\text{dil}}(\mathbf{x})}{u_{\min}} + 1 \leq 0, \\
& \frac{\mathbf{u}_2^{\text{ero}}(\mathbf{x})^T \mathbf{p}}{C_{\max}} - 1 \leq 0, \\
& \frac{\sum_{e=1}^N x_e}{NV_{\max}} - 1 \leq 0, \\
& 0 \leq x_{\min} \leq x_e \leq 1, \quad e = 1, \dots, N.
\end{aligned} \tag{4.3}$$

For the sensitivity of the objective with respect to the design variables, we look at  $\frac{\partial f}{\partial u_j}$ . Using the quotient rule, the following derivative is found:

$$\frac{\partial f}{\partial u_j} = -L_j \frac{|\mathbf{u}^{\text{tar}}| |\mathbf{L}\mathbf{u}| u_j^{\text{tar}} - \mathbf{u}^{\text{tar}} \cdot \mathbf{L}\mathbf{u} |\mathbf{u}^{\text{tar}}| \frac{1}{2|\mathbf{L}\mathbf{u}|} 2L_j u_j}{|\mathbf{u}^{\text{tar}}|^2 |\mathbf{L}\mathbf{u}|^2} \tag{4.4}$$

Finally, the sensitivities of the constraint functions should be evaluated. The constraint functions will be referred to as  $g_k$ , with  $k = 1, 2, 3$  for respectively the magnitude, compliance and volume constraints.

For the sensitivity of the magnitude constraint, please note that  $u_{\text{tip}}$  is obtained from  $\mathbf{u}$  in a similar way as in Eq. (4.2), but with a different selection vector  $\mathbf{M}$ . The sensitivities of the constraints are given below:

$$\frac{\partial g_1}{\partial u_i} = -M_i \frac{1}{M_i u_i}, \quad (4.5)$$

$$\frac{\partial g_2}{\partial u_i} = \frac{p_i}{C_{\max}}, \quad (4.6)$$

$$\frac{\partial g_3}{\partial x_e} = \frac{1}{NV_{\max}}. \quad (4.7)$$

### 4.1.3 Optimization constants

Before the first numerical example is performed the values of the different constants need to be selected. These can be found in Table 4.1 and will be further explained here. First of all, a material was chosen of which the material parameters are given in Table 4.1. This material is light weight and reasonably flexible. It is not a highly flexible material since that would make it difficult to create the stiffness that the variable-camber morphing wing needs. It was determined that for an input force  $F_{\text{in}}$  of 5 N, the tip of the wing should displace 0.01 m in vertical displacement. This ensures that for reasonable actuation forces (between 5 and 20 N) a camber of up to  $20^\circ$  can be reached. The value of the compliance constraint was chosen in such a way that for the given dynamic pressure of 245 Pa the deflection of the skin was less than 0.003 m. This is necessary to ensure that the airfoil will not deform drastically under the dynamic pressure, but will maintain its shape. The maximum allowed volume fraction  $V_{\max}$  is set to 0.1, in order to ensure the structure is light weight. The parameters of the Heaviside projection were set to  $\beta = 0.5$  and  $\mu = 0.5$ . The parameter  $x_{\min}$  is not listed in this table, since it varies between the different numerical examples. Its value will be provided for each example separately.

Table 4.1: Constant values for the topology optimization

Parameter	Value
$E$	0.4 GPa
$\nu$	0.45
$\rho$	1100 kg/m <sup>3</sup>
$F_{\text{in}}$	5 N
$u_{\text{tip}}$	0.01 m
$C_{\max}$	$1e-8$
$V_{\max}$	0.1
$\beta$	0.5
$\mu$	0.5

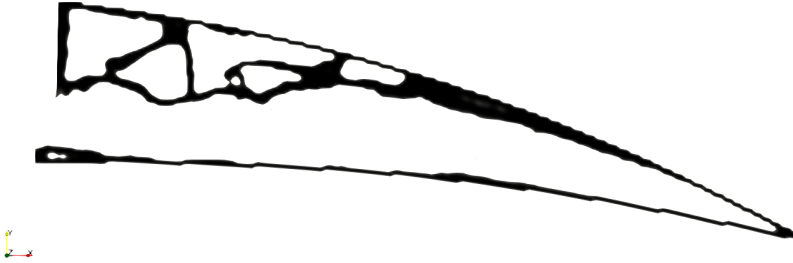
## 4.2 The influence of element densities on expected deformations

In the first numerical example, the topology optimization was performed with the constants as shown in Table 4.1 and  $x_{\min} = 0.001$ . The resulting structure of the optimization can be seen in Fig. 4.4a. The predicted deformed shape of the structure is displayed in Fig. 4.4b. The optimizer converged to an optimum where the top surface of the trailing edge has a parabolic shape. This result was then verified with the finite element software COMSOL Multiphysics. A linear 2D model was used with the exact same boundary conditions and  $F_{\text{in}}$  as were used in the topology optimization. The resulting deformed profile was plotted and is displayed in Fig. 4.5. The displacement profile as predicted by the COMSOL analysis does not match the profile predicted by the optimization. Instead of a parabolic curve, the biggest part of the displacement takes place in the tip of the profile while the first half is relatively stiff and hardly deforms at all.

It is hypothesised, that the reason for this discrepancy can be found in the void elements. The domain contains many of these elements and thus they can have a profound influence on the displacement, especially



(a) The obtained structure from the optimization with  $x_{\min} = 0.001$ .



(b) The deformed state of the structure, as approximated by the finite element analysis. Note the deformation is scaled from the linear analysis.

Figure 4.4: The obtained structure from the optimization problem as defined in Eq. (4.3) in its undeformed (a) and deformed (b) configuration.

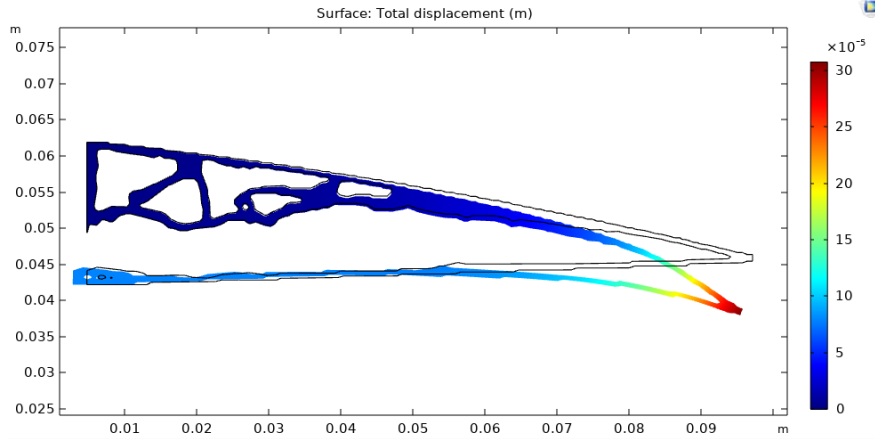


Figure 4.5: The predicted deformed configuration of the profile, calculated by COMSOL Multiphysics. Please note that the deformation is scaled, in order to make it visible. The deflection values can be found in the legend of this graph.

in a bending-based problem such as this. When the density, and thus the Young's modulus, of these void elements is not low enough, they can add significantly to the bending stiffness of the problem and therefore influence the outcome of the optimization. To test this, a simple analysis was performed on a beam in bending. This analysis will be discussed in Section 4.2.1.

#### 4.2.1 Beam in bending

To test the hypothesis that  $x_{\min}$  has a significant influence on the displacement profile, an analysis was performed for a beam in bending. In this analysis, the beam is fixed on the left side and a distributed load is imposed on the top surface (see Fig. 4.6). First, one can consider a domain which entirely consists of the beam (see Fig. 4.7a), or one can consider a larger domain in which the exact same beam is surrounded by

void elements (see Fig. 4.7b). This simple problem can be used to show the effect of void elements on the bending stiffness of a structure by analysing the tip displacement  $u_{\text{tip}}$  of the beam for different values of  $x_{\text{min}}$ . This displacement can then be compared with the tip displacement of the model of the beam without voids, to see if and how the void element density influences the displacement by evaluating:

$$\epsilon = \frac{\Delta u_{\text{tip}}}{u_{\text{tip}}^{\text{solid}}} \quad (4.8)$$

where:

$$\Delta u_{\text{tip}} = u_{\text{tip}}^{\text{solid}} - u_{\text{tip}}^{\text{void}} \quad (4.9)$$

In these equations,  $u_{\text{tip}}^{\text{solid}}$  corresponds to the tip displacement of the beam without void elements around it and  $u_{\text{tip}}^{\text{void}}$  is the tip displacement of the beam with void elements around it.  $\Delta u_{\text{tip}}$  is divided by  $u_{\text{tip}}^{\text{solid}}$  to gain a more thorough understanding of how big the difference between the displacements is as a percentage of  $u_{\text{tip}}^{\text{solid}}$ . The result of this analysis can be seen in Fig. 4.8. It is indeed true that the void element density has a significant influence on the displacement of the beam as for  $x_{\text{min}} = 0.001$  the difference is  $> 10\%$ . It is likely that this is thus also the cause of the incorrect bending profile of the morphing trailing edge. To verify that the void element densities were indeed the cause for the bad prediction of the deformed profile, the void element densities for the optimized trailing-edge were replaced by the value of  $x_{\text{min}} = 1e - 9$  in post-processing. The deformation was then calculated and is displayed in Fig. 4.9. This deformed profile is similar to the deformation as predicted by the COMSOL analysis. It is thus important to make sure that for the optimization the value of  $x_{\text{min}}$  is chosen sufficiently low, so that the stiffness of the void elements does not influence the deformation of the structure. Based on the beam in bending result a maximum value of  $x_{\text{min}} = 1e - 8$  is suggested for future optimizations.

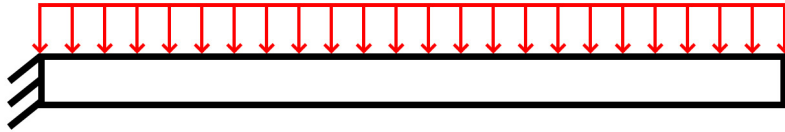


Figure 4.6: A graphical representation of the beam in bending test-case. The beam is fixed on the left, and is subjected to a distributed load.

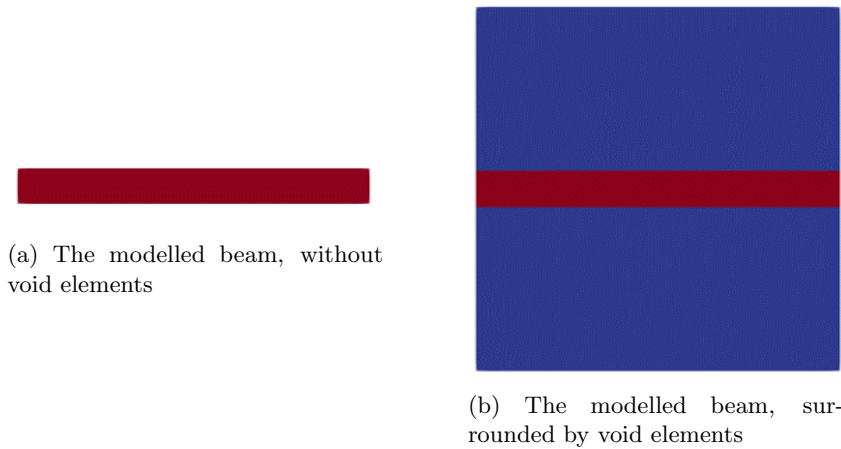


Figure 4.7: The two different models (a, b) which are used to analyse the influence of void elements on the stiffness of a beam in bending.

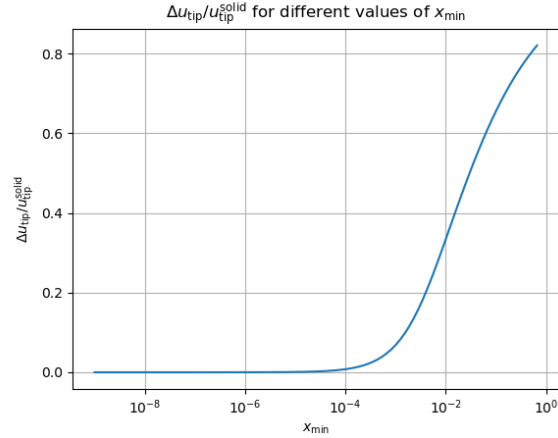


Figure 4.8: The result of the analysis. For different  $x_{\min}$ , difference in tip displacement ( $\Delta u_{\text{tip}}$ ) is displayed as a percentage of  $u_{\text{tip}}^{\text{solid}}$ , between the model with an without void elements.



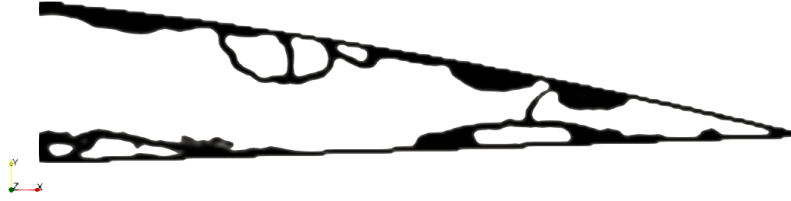
Figure 4.9: The expected deformed profile of the optimized trailing edge for  $x_{\min} = 1e - 9$ . Note the deformation is scaled from the linear analysis.

### 4.3 Final design

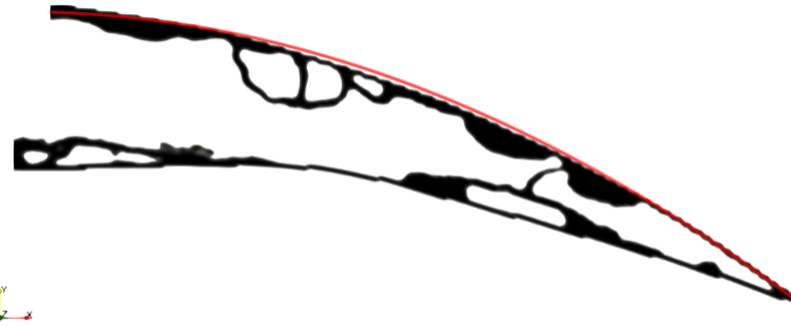
For this numerical example, the topology optimization was performed with a minimal density value of  $x_{\min} = 1e - 8$ . The design that was obtained from the optimization and its expected deformed state can be found in Fig. 4.10. This profile complied with all constraints and it shows the quadratic deformed shape that was aimed for, with only a small deviation roughly in the middle of the shape. This deviation, where the obtained shape is slightly less convex than the desired shape, is caused by the stiffness of the structure. To further assess this result, its deformed state was compared to a COMSOL model of the same profile and an eigenvalue analysis was done to gain a better understanding of the behaviour of the structure when the actuator is either active or fixed. This can give information both about the stiffness of the structure and about the deformation modes one might expect to see.

First, the structure was imported in COMSOL and its deformation calculated. This result can be seen in Fig. 4.11. Notably, COMSOL shows the parabolic shape of the deformed top surface, indicating that the prediction of the deformed state in the topology optimization is accurate. Also, for an input force of 5 N the total tip displacement as predicted by COMSOL is 0.010907 m, this complies with the magnitude constraint set in the optimization and indicates that the profile can be actuated with low actuation forces.

Second, the eigenvalue analysis was performed. First with the actuator input free, to see what the



(a) The undeformed trailing-edge, as obtained by the topology optimization.



(b) The deformed state of the trailing-edge, as predicted by the optimization. The red line indicates the desired, quadratic shape. Note the deformation is scaled from the linear analysis.

Figure 4.10: The obtained trailing-edge in its neutral (a) and deformed (b) configurations.

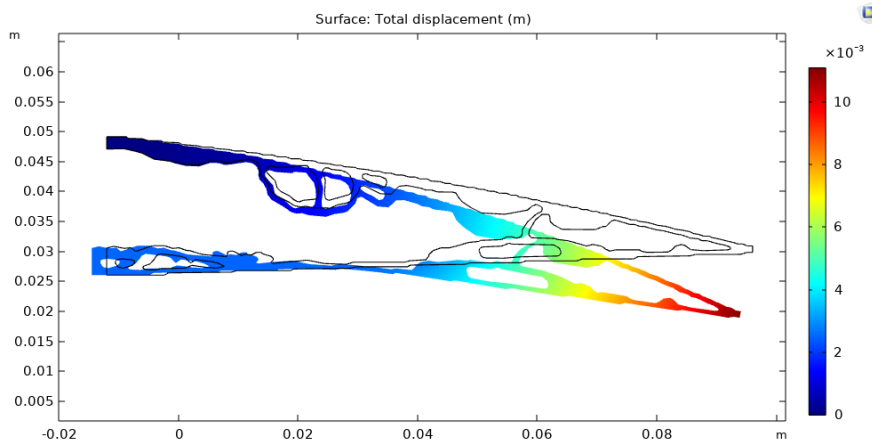


Figure 4.11: The deformed profile as calculated by COMSOL. The colour map represents the amount of displacement in [m].

eigenfrequency of the desired deformation mode is and what other modes are that might be excited and how their stiffness is as compared to the desired deformation mode. Next, the modes of the structure when the actuator input is fixed are analyzed, to see what kind of frequencies would interfere with the trailing-edge while it is fixed in a certain state.

For the eigenvalue analysis with the free actuator input it was found that the first eigenmode is the desired deformation mode and that it is located at an eigenfrequency of  $\lambda_1 = 21.9$  Hz. This indicates that this mode is flexible and will require low actuation energy. This would also make the design suitable for an active turbulence damping application. In such an application, the wing would be actuated in order to actively dampen in-flight turbulence. This would have many advantages such as less wake turbulence at take-off and landing, more comfort and better safety. For this type of damping, the actuation frequency is

often up to 20 Hz since these are the frequencies at which turbulence is most severe [39]. This is also near the frequency of the desired deformation mode, making it very energy efficient to actuate the system. The other eigenfrequencies of the structure are in the range of 100 – 325 Hz, indicating that these modes are significantly stiffer than the desired deformation mode and will not interfere with the actuation. For the precise eigenfrequencies and mode shapes corresponding to those frequencies, see Appendix B.

If the actuation input is completely fixed, the first eigenfrequency is at  $\mu_1 = 71.3$  Hz, which is relatively low as compared to the other eigenfrequencies in this case, that are in the range of 200 – 400 Hz. These are stiff modes and unlikely to cause problems. The mode shapes and exact frequencies can be found in Appendix B. As mentioned before, airflow turbulence is most severe at low frequencies of up to 20 Hz. It is therefore unlikely that the first eigenmode here will cause issues with respect to turbulence. It might however interfere with aero-elasticity phenomena such as flutter and buffeting, but this is outside of the scope of this thesis.

It was observed during the numerical examples that there is a big trade-off between the stiffness and the obtained output shape of the wing. When the required stiffness was increased, the shape suffered. This also shows that it is very complex to have both the required stiffness and flexibility of the profile with the allotted maximum amount of material.

In conclusion, the obtained design seems to be a promising candidate for a morphing trailing edge, as it shows the desired displacement profile and complies with the different demands of a morphing wing. Including the skin in the design might have increased the complexity of the optimization, but it did not obstruct the possibility of a promising design. Including the skin resolves the problem of designing a separate morphing skin and allowed us to include the compliance of this part as well. The optimal design was 3D printed and tested, to see if it shows the same promising qualities in real life as predicted by the optimization. The experimental validation can be found in the following Chapter.



## Chapter 5

# Experimental validation

A prototype of the designed variable-camber morphing wing was 3D printed and it was assessed whether the deformed shape of the prototype matched the output shape as predicted by the linear analysis in the optimization. The wing was printed using RS TPC Flex 45 filament, a highly flexible material with  $E = 95$  MPa. This is a different material than included in the topology optimization, as the latter material was unavailable. The 3D printed structure was based on a total chord length of 38 cm and the total length of the designed trailing-edge is therefore 19 cm. This scaling was necessary to ensure that the 3D printers minimal feature size would not interfere with the small connections in the trailing edge.

The experimental set-up is depicted in Fig. 5.1. Various deformed shapes, as predicted by the linear analysis that was part of the optimization, were colour coded and printed. These predicted deformed shapes ranged from blue, which is the neutral position of the trailing edge, green with a deflection angle of  $6^\circ$  and yellow with a deflection angle of  $12^\circ$ . The deflection angle keeps increasing with steps of  $6^\circ$  until the final grey profile with a deflection angle of  $30^\circ$ . The deflection angle is defined as the angle between a horizontal line, drawn from the top of the neutral (blue) state and a line from the tip of the deformed profile to the place where the horizontal line intersects the middle of the airfoil profile. The prototype of the variable-camber morphing wing was fixed on the top left and the bottom left was mounted on a slider. Using the slider, the prototype was deformed until the tip displacement matched that of one of the coloured predicted deformed shapes. The profile of the prototype was then compared to the profile of that predicted deformed shape. This process was repeated for all coloured predicted deformed shapes. It was hypothesized that for small deformations (represented by the green and yellow predicted profiles) the profile of the prototype would match the predicted profiles, while for larger deformations (represented by the red, black and grey predicted profiles) the profile of the prototype would start to differ from the predicted profiles as linear modeling assumptions become less valid with increased deformation. In this chapter only the pictures needed to support the conclusions that are drawn are included, for the complete set of pictures of the experiment, see Appendix C.

It was found that the deformed prototype matched the green predicted deformed profile (see Fig. 5.2). However, from the yellow predicted profile onwards the profile of the prototype did not match the predicted profiles perfectly, see for example Fig. 5.3 where the prototype is deformed according to the black profile. The prototype appears stiffer than expected as the deformed top surface of the prototype is less convex than the predicted profiles. This could be caused by the fact that the slider allowed for some rotation of the bottom surface of the prototype. Additionally, it is possible that non-linear effects come into play when larger deformations are reached. Apart from small differences in convexity of the top surface of the prototype however, the deformation profile of the prototype showed a quadratic-like behaviour that could result in superior performance during flight as compared to the traditional flap system.

It should be noted that, for large deformations, the slider structure experiences relatively large forces perpendicular (in-plane) to the sliding direction. This is due to the inclination of the bottom surface to rotate when deformed. The slider connection blocks this rotation, but does experience a force because of it. In the prototype set-up, this caused problems because from a certain amount of deformation onwards, the slider blocks itself. For future prototypes it is therefore recommended to use a slider or linear bearing that is capable of dealing with these counter forces without blocking.



Figure 5.1: The set-up for testing the predicted output shape. The 3D printed model is fixed on the top left corner. The bottom left is fixed to a slider which slides through a metal profile. Behind the prototype, a print out of expected output shapes is attached for different degrees of deformation.



Figure 5.2: The prototype deformed according to the green profile, with an angle of  $6^\circ$  with respect to the neutral camber line.

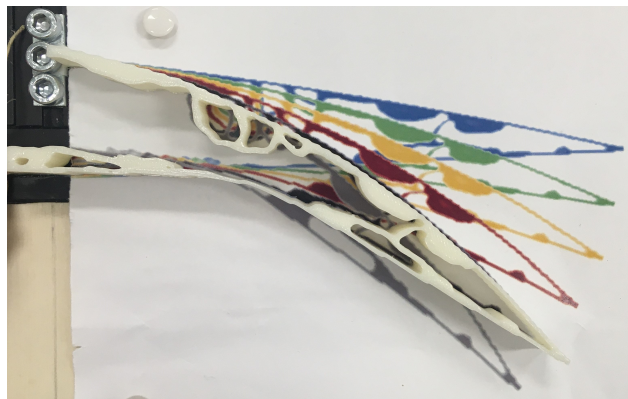


Figure 5.3: The prototype deformed according to the black profile, with an angle of  $24^\circ$  with respect to the neutral camber line.

# Chapter 6

## Conclusions and recommendations

### 6.1 Conclusions

The design of variable-camber morphing wing is an active topic of research. This is a challenging design problem because of the three inherently contradictory properties that are desired in a variable-camber morphing wing namely flexibility, stiffness and a light-weight structure. Compliant mechanisms are a promising candidate for application in a variable-camber morphing wing. The aim of this thesis was to design a compliant variable-camber morphing wing using density based topology optimization. In the optimization, the wing skin was included as a non-design domain. Including the wing skin as a part of the designed mechanism solves not only the problem of the variable-camber morphing wing design, but also the challenging design problem of a morphing skin.

The method presented in this thesis for the density-based topology optimization of compliant shape-morphing structure, has shown to be able to obtain shape-morphing structures that adhere well to the prescribed shape changes. The proposed objective function is a dot-product which focuses purely on the output shape, while the magnitude of the output displacement is filtered out. This novel objective function formulation based on a dot-product has much quicker convergence to the optimum than a LSE objective does. This results in superior performance (i.e. the obtained structures with the dot-product objective comply with the desired output shape better than the structures obtained with the LSE objective) of optimizations using the dot-product objective function, especially when the optimized problem becomes more complex involving multiple input-output relations or multiple contradictory constraints. This makes the dot-product objective function a good candidate for application in the optimization of shape-morphing structures.

It has been shown that, in 2D, the proposed method produces good results for the variable-camber morphing wing design problem: a design of the variable-camber morphing wing was obtained that resulted in a quadratic deformed shape of the top surface, while it was also stiff enough to withstand the pressures present during flight. It is important that the densities of the void elements are chosen sufficiently low to avoid that these elements influence the stiffness of the obtained structure. It should be noted that the required stiffness and the obtained output shape of the morphing wing are a trade-off. It was observed that as soon as the required stiffness was increased, the obtained output shape of the profile became less quadratic-like.

A prototype of the obtained design for the morphing trailing edge was 3D printed and tested to see if the deformed shape of the prototype was as predicted by the linear analysis. This was checked for different linear scalings of the deformed profile as expected by the linear analysis, ranging from small deformations to much larger deformations. The prototype performed well, i.e. the deformed shape matched the predicted deformed shapes well. When the deformation increases, some deviation is seen as the deformed shape of the prototype is slightly less convex than the expected deformed shape. This is probably caused by two things. First, the slider has some play which allowed some rotation of the bottom surface of the wing. This might influence the deformed profile. Additionally, when the deformation is bigger it is probable that non-linearities come into play which may cause the prototype to differ from the predicted profile, since for the analysis linearity was assumed.

In sum, the topology optimization of a compliant variable-camber morphing wing that includes the morphing skin has proved to be an effective method that can obtain compliant shape-morphing structures that

adhere well to required shape changes well. The dot-product objective function performs well, with quick convergence to an optimum. The experimental validation shows that the obtained structure behaves as predicted by the optimization for small deformations.

## 6.2 Recommendations for future research

Based on the work presented here several recommendations can be made for future research. First, it is recommended that the methodology presented in this thesis is extended to a 3D topology optimization for a variable-camber morphing wing. It is hypothesized that when performing a 3D topology optimization it becomes easier to obtain a quadratic output shape while maintaining stiffness due to the optional asymmetrical placement of stiffening structures in spanwise direction. 3D modelling also has the advantage that the entire trailing edge can be modelled, instead of only a cross-section. Aero-elasticity analysis should be considered in the model as well, since effects such as flutter and buffeting are important to consider as they can cause serious flight hazards when unaccounted for.

With respect to the production and testing of prototypes, it is recommended that the prototype is printed using the material it was designed with. Furthermore, it is recommended that not only the deformed shape of the prototype is assessed, but also the aerodynamic performance of the prototype is tested. This could be done by performing windtunnel experiments, during which one can see what influence a compliant variable-camber morphing wing has on lift- and drag coefficients. This would allow for the option to test the design for stiffness under different dynamic pressures and other elasticity effects.

# Bibliography

- [1] NASA. (2021). “Wing geometry definitions.” 04-07-2021, [Online]. Available: <https://www.grc.nasa.gov/www/k-12/airplane/geom.html>.
- [2] B. Woods, O. Bilgen, and M. Friswell, “Wind tunnel testing of the fish bone active camber morphing concept,” *Journal of Intelligent Material Systems and Structures*, vol. 25, no. 7, pp. 772–785, 2014. DOI: 10.1177/1045389X14521700.
- [3] W. Kang, E. Kim, M. Jeong, and I. Lee, “Morphing wing mechanism using an sma wire actuator,” *int’l J. of Aeronautical & Space Sci.*, vol. 13, no. 1, pp. 58–63, 2012. DOI: 10.5139/IJASS.2012.13.1.58.
- [4] C. Thill, J. Etches, I. Bond, K. Potter, and P. Weaver, “Morphing skins,” *The Aeronautical Journal*, pp. 117–139, 2008.
- [5] S. Barbarino, O. Bilgen, R. Ajaj, M. Friswell, and D. Inman, “A review of morphing aircraft,” *Journal of Intelligent Material Systems and Structures*, vol. 22, no. 9, pp. 823–877, 2011. DOI: 10.1177/1045389X11414084.
- [6] C. Taylor, “Flight test results of a trailing edge flap designed for direct-lift control,” NASA, Tech. Rep., Oct. 1969.
- [7] S. Kota, J. Hetrick, R. Osborn, D. Paul, E. Pendleton, P. Flick, and C. Tilmann, “Design and application of compliant mechanisms for morphing aircraft structures,” in *Smart Structures and Materials 2003: Industrial and Commercial Applications of Smart Structures Technologies*, E. H. Anderson, Ed., International Society for Optics and Photonics, vol. 5054, SPIE, 2003, pp. 24–33. DOI: 10.1117/12.483869.
- [8] B. Li and G. Li, “Analysis and optimization of a camber morphing wing model,” *International Journal of Advanced Robotic Systems*, vol. 13, 2016. DOI: 10.1177/1729881416664846.
- [9] A. Dale, J. Cooper, and A. Mosquera, “Topology optimization & Experimental Validation of 0-v Honeycomb for adaptive morphing wing,” in *22nd AIAA/ASME/AHS Adaptive Structures Conference*, [13 - 17 January, 2014, National Harbor, Maryland], 2014.
- [10] J. Sun, Q. Guan, Y. Liu, and J. Leng, “Morphing aircraft based on smart materials and structures: A state-of-the-art review,” *Journal of Intelligent Material Systems and Structures*, vol. 27, no. 17, pp. 2289–2312, 2016.
- [11] K. Lu and S. Kota, “Design of compliant mechanisms for morphing structural shapes,” *Journal of Intelligent Material Systems and Structures*, vol. 14, pp. 379–391, 2003. DOI: 10.1177/1045389X03035563.
- [12] A. Hasse and L. Campanile, “Design of compliant mechanisms with selective compliance,” *Smart materials and structures*, vol. 18, no. 11, 2009. DOI: 10.1088/0964-1726/18/11/115016.
- [13] A. Hasse, I. Zuest, and L. Campanile, “Modal synthesis of belt-rib structures,” *proc. inst. of mechanical engineers part C: Journal of mechanical engineering science*, vol. 225, no. 3, pp. 722–732, 2010. DOI: 10.1243/09544062JMES2329.
- [14] A. Hasse, M. Franz, and K. Mauser, *Synthesis of compliant mechanisms with defined kinematics*. Springer International Publishing Switzerland, 2017, pp. 227–238, In: Microactuators and micromechanisms.
- [15] L. Cao, A. Dolovich, and W. Zhang, “On understanding of design problem formulation for compliant mechanisms through topology optimization,” *Mechanical Sciences*, vol. 4, no. 2, pp. 357–369, 2013. DOI: 10.5194/ms-4-357-2013.

- [16] R. Haftka and Z. Gürdal, *Elements of Structural Optimization*. Springer Science + Business Media, 1992.
- [17] M. Bendsoe and O. Sigmund, *Topology Optimization: Theory, Methods and Applications*. Springer, 2003, ISBN: 3-540-42992-1.
- [18] P. Christensen and A. Klarbring, *An Introduction to Structural Optimization*. Springer Science + Business Media, 2009, Solid mechanics and it's applications series, volume 153.
- [19] Y. Zhang, W. Ge, Z. Zhang, X. Mo, and Y. Zhang, "Design of compliant mechanism-based variable camber morphing wing with nonlinear large deformation," *International Journal of Advanced Robotic Systems*, vol. 16, no. 6, 2019. DOI: 10.1177/1729881419886740.
- [20] K. Svanberg, "The method of moving asymptotes—a new method for structural optimization," *International Journal for Numerical Methods in Engineering*, vol. 24, no. 2, pp. 359–373, 1987. DOI: 10.1002/nme.1620240207.
- [21] S. Koppen, "Topology optimization of optomechanical systems," M.S. thesis, Delft University of Technology, 2017.
- [22] K. Lu and S. Kota, "Synthesis of shape morphing compliant mechanisms using load path representation method," in *Proc. SPIE 5049*, [Smart Structures and Materials, San Diego, California], 2003.
- [23] M. Santer and S. Pellegrino, "Topological optimization of compliant adaptive wing structure," *AIAA Journal*, vol. 47, no. 3, pp. 523–534, 2009. DOI: 10.2514/1.36679.
- [24] A. Hasse and F. Campanile, "Synthesis of Compliant Mechanisms for Shape Adaptation by means of a Modal Procedure," in *19th International Conference on Adaptive Structures and Technologies*, [6 - 9 October, Ascona, Switzerland], 2008.
- [25] X. Tong, W. Ge, C. Sun, and X. Liu, "Topology optimization of compliant adaptive wing leading edge with composite materials," *Chinese Journal of Aeronautics*, vol. 27, no. 6, pp. 1488–1494, 2014. DOI: 0.1016/j.cja.2014.10.015.
- [26] K. Maute and G. W. Reich, "Integrated multidisciplinary topology optimization approach to adaptive wing design," *Journal of Aircraft*, vol. 43, no. 1, pp. 253–263, 2006. DOI: 10.2514/1.12802.
- [27] C. Thill, J. Etches, I. Bond, K. Potter, P. Weaver, *et al.*, "Morphing skins," *The aeronautical journal*, vol. 112, no. 1129, pp. 117–139, 2008.
- [28] P. D. L. Jensen, F. Wang, I. Dimino, and O. Sigmund, *Topology optimization of large-scale 3d morphing wingstructures*, 2021. DOI: 10.20944/preprints202107.0051.v1.
- [29] E. Fernández, K. Yang, S. Koppen, P. Alarcón, S. Bauduin, and P. Duysinx, "Imposing minimum and maximum member size, minimum cavity size, and minimum separation distance between solid members in topology optimization," *Computer Methods in Applied Mechanics and Engineering*, vol. 368, p. 113 157, 2020. DOI: <https://doi.org/10.1016/j.cma.2020.113157>.
- [30] O. Sigmund, "Manufacturing tolerant topology optimization," *Acta Mech Sin*, vol. 25, pp. 227–239, 2009. DOI: 10.1007/s10409-009-0240-z.
- [31] E. Andreassen, A. Clausen, M. Schevenels, B. Lazarov, and O. Sigmund, "Efficient topology optimization in matlab using 88 lines of code," *Struct Multidisc Optim*, vol. 43, pp. 1–16, 2011. DOI: 10.1007/s00158-010-0594-7.
- [32] D. A. Tortorelli and P. Michaleris, "Design sensitivity analysis: Overview and review," *Inverse Problems in Engineering*, vol. 1, no. 1, pp. 71–105, 1994. DOI: 10.1080/174159794088027573.
- [33] MathWorks. (2021). "Fmincon." 18-06-2021, [Online]. Available: <https://nl.mathworks.com/help/optim/ug/fmincon.html>.
- [34] *Design Approach for Selection of Wing Airfoil with Regard to micro-UAVs*, Proceedings of the International Micro Air Vehicles conference, 2011, pp. 126–131. DOI: 10.4233/uuid:2b261a19-fae4-44dd-ac04-1113ebc7c89b.
- [35] NASA. (2021). "Dynamic pressure." 09-06-2021, [Online]. Available: <https://www.grc.nasa.gov/www/k-12/airplane/dynpress.html>.

- [36] *Preliminary Investigation of a Fishbone Active Camber Concept*, vol. Volume 2: Mechanics and Behavior of Active Materials; Integrated System Design and Implementation; Bio-Inspired Materials and Systems; Energy Harvesting, Smart Materials, Adaptive Structures and Intelligent Systems, 2012, pp. 555–563. DOI: 10.1115/SMASIS2012-8058.
- [37] B. Sanders, F. E. Eastep, and E. Forster, “Aerodynamic and aeroelastic characteristics of wings with conformal control surfaces for morphing aircraft,” *Journal of Aircraft*, vol. 40, no. 1, pp. 94–99, 2003. DOI: 10.2514/2.3062.
- [38] D. Hunsaker, J. Reid, and J. Joo, “Geometric definition and ideal aerodynamic performance of parabolic trailing-edge flaps,” *International Journal of Astronautics and Aeronautical Engineering*, vol. 4, pp. 1–17, Mar. 2019. DOI: 10.35840/2631-5009/7526.
- [39] A. Galfy, R. Gaggl, R. Mühlbacher, D. Frank, J. Schlarp, and G. Schitter, “Turbulence load prediction for manned and unmanned aircraft by means of anticipating differential pressure measurements,” *CEAS Aeronautical Journal*, 2021. DOI: 10.1007/s13272-021-00512-y.

# Appendix A

## Matlab code

### A.0.1 Variables k

```
1 %% This matlab file contains a simple analysis of LSE vs Dot-product
2 % model: 2 linear springs in series
3 clear, close all
4
5 %% setting parameter values
6 umin = 0.15;           % Minimum amount of displacement for magnitude constraint
7 F = 1;                 % Force of 1 N on end
8 utar = [0.1 ; 0.15];  %target displacements of the nodes
9
10 %% Optimization with fmincon for LSE
11 % set the options of fmincon
12 options = optimoptions('fmincon','Display','iter','Algorithm','sqp', ...
    'OutputFcn',@outputFcn_global);
13 f_LSE = @LSE;
14 k = fmincon(f_LSE, [1, 1], [], [], [], [], [1, 1], [50,50], [], options)
15
16 % obtain output data of every iteration
17 global outputFcn_global_data
18 Values =[outputFcn_global_data.x];
19 k1_LSE = [];
20 k2_LSE = [];
21
22 % Store the spring stiffnesses at each iteration in vectors
23 for i = 1:length(Values)
24     if rem(i, 2) == 0
25         k2_LSE(end+1) = Values(i);
26         eLSE
27         k1_LSE(end+1) = Values(i);
28     end
29 end
30
31 %% optimization with fmincon for dot
32 % Set options for fmincon
33 options = optimoptions('fmincon','Display','iter','Algorithm','sqp', ...
    'OutputFcn',@outputFcn_global);
34 nonlincon = @dotconstraints;
35 f_dot=@DOT;
36 q = fmincon(f_dot, [1, 1], [], [], [], [], [], [], [], nonlincon, options)
37
38 % obtain output data of every iteration
39 global outputFcn_global_data
40 Values =[outputFcn_global_data.x];
41 k1_dot = [];
42 k2_dot = [];
43
44 % Store the spring stiffnesses at each iteration in vectors
```

```

45 for i = 1:length(Values)
46     if rem(i, 2) == 0
47         k2_dot(end+1) = Values(i);
48         eLSE
49         k1_dot(end+1) = Values(i);
50     end
51 end
52
53 %% Create the functions that need to be plotted
54 % Grid of values for k_1 and k_2
55 K1 = linspace(1, 50, 100);
56 K2 = linspace(1, 50, 100);
57 [k1_plot, k2_plot] = meshgrid(K1, K2);
58
59 % Values of the different objectives and constraints on this grid
60 f_LSE_plot = sqrt((F./k1_plot) - u_tar(1)).^2 + ((F*((1./k1_plot) + (1./k2_plot))- ...
    u_tar(2)).^2);
61 f_dot_plot = 1-(u_tar(1).* (F./k1_plot) + u_tar(2)* F*((1./k1_plot) + ...
    (1./k2_plot)))/(sqrt(u_tar(1)^2+u_tar(2)^2)*sqrt((F./k1_plot).^2 + (F*((1./k1_plot) ...
    + (1./k2_plot)).^2));
62 g2_mag = -(F*((1./k1_plot) + (1./k2_plot)))/umin) +1;
63
64
65 %% Create Contour plots
66 figure
67 hold on
68 contour(k1_plot, k2_plot, f_LSE_plot, [0 .0500 .01000 .02000 .1 .5000], 'showtext', 'on');
69 plot(k1_LSE, k2_LSE, '*')
70 title('LSE objective function with iteration values')
71 xlabel('k_1')
72 ylabel('k_2')
73 legend('f_{LSE}', 'Iterations values for k_1 and k_2')
74
75
76 figure
77 hold on
78 contour(k1_plot, k2_plot, f_dot_plot, [0.0 0.0 0.0001 0.001 .0500 .01000 .02000 .1 .5000], ...
    'showtext', 'on')
79 contour(k1_plot, k2_plot, g2_mag, [0.0 0.0], 'LineColor', 'b', 'LineWidth', 2);
80 plot(k1_dot, k2_dot, '*')
81 title('Dot-product objective function with constraint and iteration values')
82 xlabel('k_1')
83 ylabel('k_2')
84 legend('f_{LSE}', 'g_{mag}', 'Iterations for k_1 and k_2')
85
86 %% Functions for optimizations
87 % LSE objective function
88 function [f_LSE]=LSE(k)
89 F = 1;
90 u_tar = [0.1 ; 0.15];
91 f_LSE = sqrt((F/k(1)-u_tar(1))^2 + (F/(1/((1/k(1))+1/k(2))))-u_tar(2))^2)/2;
92 end
93
94 % dot-product objective function
95 function [f_dot] = DOT(q)
96 F = 1;
97 u_tar = [0.1; 0.15];
98 f_dot = 1 - ((u_tar(1)*F/q(1)+ ...
    u_tar(2)*F/(1/((1/q(1))+1/q(2)))))/(sqrt((F/q(1))^2+(F/(1/((1/q(1))+1/q(2))))^2)*
99 sqrt((u_tar(1))^2+(u_tar(2))^2));
100 end
101
102 % non-linear constraints of dot-product objective
103 function [c, ceq] = dotconstraints(q)
104 F = 1;
105 umin = 0.15;
106 ceq(1) = -(F/(1/((1/q(1))+1/q(2))))+umin;
107 c=[];

```

## A.0.2 Variables x

```

1 %% This matlab file contains a simple analysis of LSE vs Dot-product
2 % model: 2 linear springs in series
3 clear, close all
4
5 %% setting parameter values
6 umin = 0.15; % Minimum amount of displacement for magnitude constraint
7 F = 1; % Force of 1 N on end
8 utar = [0.1 ; 0.15]; %target displacements of the nodes
9
10 %% Optimization with fmincon for LSE
11 % set the options of fmincon
12 options = optimoptions('fmincon','Display','iter','Algorithm','sqp', ...
    'OutputFcn',@outputFcn_global);
13 f_LSE = @LSE;
14 % nonlincon = @LSEconstraints;
15 k = fmincon(f_LSE, [1, 1], [], [], [], [], [1, 1], [50,50], [], options)
16
17 % obtain output data of every iteration
18 global outputFcn_global_data
19 Values =[outputFcn_global_data.x];
20 k1_LSE = [];
21 k2_LSE = [];
22
23 % Store the spring stiffnesses at each iteration in vectors
24 for i = 1:length(Values)
25     if rem(i, 2) == 0
26         k2_LSE(end+1) = Values(i);
27         eLSE
28         k1_LSE(end+1) = Values(i);
29     end
30 end
31
32 %% optimization with fmincon for dot
33 % Set options for fmincon
34 options = optimoptions('fmincon','Display','iter','Algorithm','sqp', ...
    'OutputFcn',@outputFcn_global);
35 nonlincon = @dotconstraints;
36 f_dot=@DOT;
37 q = fmincon(f_dot, [1, 1], [], [], [], [], [1, 1], [], [], nonlincon, options)
38
39 % obtain output data of every iteration
40 global outputFcn_global_data
41 Values =[outputFcn_global_data.x];
42 k1_dot = [];
43 k2_dot = [];
44
45 % Store the spring stiffnesses at each iteration in vectors
46 for i = 1:length(Values)
47     if rem(i, 2) == 0
48         k2_dot(end+1) = Values(i);
49         eLSE
50         k1_dot(end+1) = Values(i);
51     end
52 end
53
54 %% Create the functions that need to be plotted
55 % Grid of values for k_1 and k_2
56 K1 = linspace(1, 5, 100);
57 K2 = linspace(1, 5, 100);
58 [k1_plot, k2_plot] = meshgrid(K1, K2);
59

```

```

60 % Values of the different objectives and constraints on this grid
61 f_LSE_plot = sqrt(((F./(k1_plot.^3)) - u_tar(1)).^2 + ((F*(1./(k1_plot.^3)) + ...
    (1./(k2_plot.^3)))- u_tar(2)).^2);
62 f_dot_plot = 1-(u_tar(1).* (F./(k1_plot.^3)) + u_tar(2)* F*((1./(k1_plot.^3)) + ...
    (1./(k2_plot.^3)))/
63 (sqrt(u_tar(1)^2+u_tar(2)^2)*sqrt(((F./(k1_plot.^3)).^2 + (F*(1./(k1_plot.^3)) + ...
    (1./(k2_plot.^3)).^2));
64 g2_mag = -((F*(1./(k1_plot.^3)) + (1./(k2_plot.^3)))/umin) +1;
65
66
67 %% Create Contour plots
68 figure
69 hold on
70 contour(k1_plot, k2_plot, f_LSE_plot, [0 .0500 .01000 .02000 .1 .5000], 'showtext', 'on');
71 plot(k1_LSE,k2_LSE, '*')
72 title('LSE objective function with constraints and iteration values')
73 xlabel('x_1')
74 ylabel('x_2')
75 legend('f_{LSE}', 'Iterations values for x_1 and x_2')
76
77
78 figure
79 hold on
80 contour(k1_plot, k2_plot, f_dot_plot, [0.0 0.0 0.0001 0.001 .0500 .01000 .02000 .1 .5000], ...
    'showtext', 'on')
81 contour(k1_plot, k2_plot, g2_mag, [0.0 0.0], 'LineColor', 'b', 'LineWidth', 2);
82 plot(k1_dot, k2_dot, '*')
83 title('Dot-product objective function with constraints and iteration values')
84 xlabel('x_1')
85 ylabel('x_2')
86 legend('f_{dot}','g_{mag}', 'Iteration values for x_1 and x_2')
87
88 %% Functions for optimizations
89 % LSE objective function
90 function [f_LSE]=LSE(k)
91 F = 1;
92 u_tar = [0.1 ; 0.15];
93 f_LSE = sqrt((F/(k(1)^3)-u_tar(1))^2 + (F/(1/((1/(k(1)^3))+1/(k(2)^3))))-u_tar(2))^2)/2;
94 end
95
96 % dot-product objective function
97 function [f_dot] = DOT(q)
98 F = 1;
99 u_tar = [0.1; 0.15];
100 f_dot = 1 - ((u_tar(1)*F/(q(1)^3)+ ...
    u_tar(2)*F/(1/((1/(q(1)^3))+1/(q(2)^3)))))/(sqrt((F/(q(1)^3))^2+(F/(1/((1/(q(1)^3))+1/(q(2)^3))))^2)*
101 sqrt((u_tar(1))^2+(u_tar(2))^2));
102 end
103
104 % non-linear constraints of dot-product objective
105 function [c, ceq] = dotconstraints(q)
106 F = 1;
107 umin = 0.15;
108 ceq(1) = -(F/(1/((1/(q(1))^3)+(1/(q(2)^3)))))+umin;
109 c=[];
110 end

```

### A.0.3 Multiple springs

```

1 %% This matlab file contains a simple analysis of LSE vs Dot-product
2 % model: 2 linear springs in series
3 clear, close all
4
5 %% setting parameter values
6 N=500 % Number of springs in series

```

```

7 F = 1; % Force of 1 N on end node
8 u_tar = randomu(N); % Target displacements of the nodes, randomized increasing between 0 ...
    and 1
9 start = ones(1,N); % Vector with starting point for optimization
10
11 %% Optimization with fmincon for LSE
12 % set the options of fmincon
13 options = ...
    optimoptions('fmincon','Display','iter','Algorithm','sqp','MaxFunctionEvaluations', ...
        500000, 'MaxIterations', 10000);
14 f_LSE = @(k) LSE(k, F, u_tar, N);
15 % nonlincon = @LSEconstraints;
16 k = fmincon(f_LSE, start, [], [], [], [], [], [], [], options)
17
18 %% optimization with fmincon for dot
19 % Set options for fmincon
20 options = optimoptions('fmincon','Display','iter','Algorithm','sqp', ...
    'MaxFunctionEvaluations', 500000, 'MaxIterations', 10000);
21 nonlincon = @(q) dotconstraints(q, F, u_tar, N);
22 f_dot=@(q) DOT(q, F, u_tar, N);
23 q = fmincon(f_dot, start, [], [], [], [], [], [], nonlincon, options)
24
25 %% Functions for optimizations
26
27 % LSE objective function
28 function [f_LSE]=LSE(k, F, u_tar, N)
29 for i=1:N
30     for j=1:i
31         k_part(j) = 1/(k(j)^3);
32     end
33     keq(i) = sum(k_part);
34 end
35
36 for m=1:N
37     LSE_part(m) = (F*keq(m)-u_tar(m))^2;
38 end
39
40 f_LSE = sqrt(sum(LSE_part))/N;
41 end
42
43 % dot-product objective function
44 function [f_dot] = DOT(q, F, u_tar, N)
45 for i=1:N
46     for j=1:i
47         k_part(j) = 1/(q(j)^3);
48     end
49     keq(i) = sum(k_part);
50 end
51
52 for m=1:N
53     num(m) = u_tar(m)*F*keq(m);
54     den_tar(m) = u_tar(m)^2;
55     den_var(m) = (F*keq(m))^2;
56 end
57
58 f_dot = 1 - ((sum(num))/(sqrt(sum(den_tar))*sqrt(sum(den_var))));
59 end
60
61 % non-linear constraints of dot-product objective
62 function [c, ceq] = dotconstraints(q, F, u_tar, N)
63 u_min = u_tar(N);
64
65 for i=1:N
66     for j=1:i
67         k_part(j) = 1/(q(j)^3);
68     end
69     keq(i) = sum(k_part);
70 end

```

```
71
72 ceq(1) = -(F*keq(N))+umin;
73 c=[];
74 end
75
76 %Set up randomized u_tar
77 function [u_tar] = randomu(N)
78 u_tar = sort((1-0.001)*rand(N,1), 'ascend')
79 end
```

# Appendix B

## Eigenfrequency analysis

Table B.1: The eigenfrequencies and modes in the case where the actuator input is free

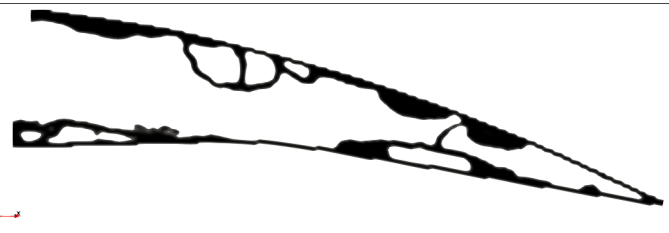
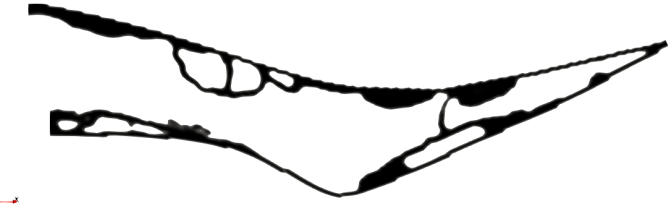
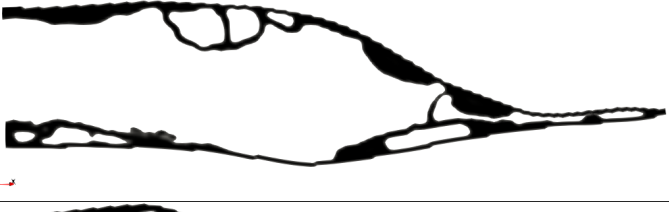
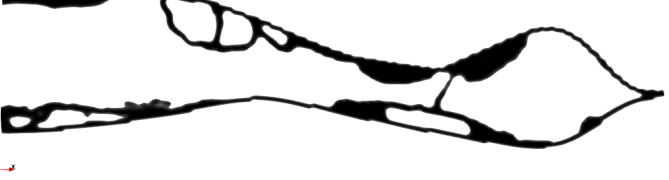
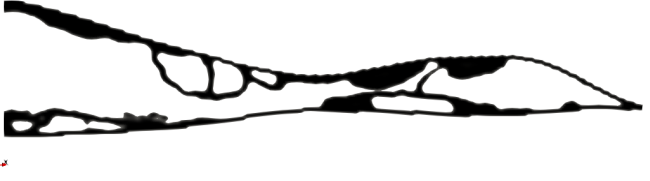
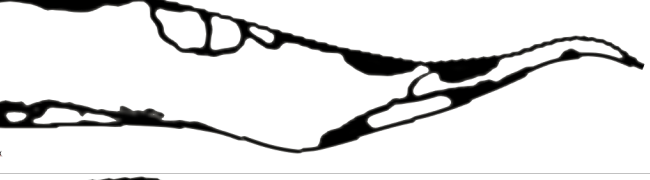
Eigenfrequency $\lambda_i$	Eigenmode
$\lambda_1 = 21.9$ Hz	 The eigenmode shape for $\lambda_1 = 21.9$ Hz shows a cross-section of a tapered beam with a central cutout. The beam is oriented horizontally. The mode shape is characterized by a slight upward curvature of the upper surface and a slight downward curvature of the lower surface, with a small displacement at the tip. A small 3D coordinate system with x, y, and z axes is shown at the bottom left of the mode shape.
$\lambda_2 = 98.7$ Hz	 The eigenmode shape for $\lambda_2 = 98.7$ Hz shows a cross-section of a tapered beam with a central cutout. The beam is oriented horizontally. The mode shape is characterized by a significant upward curvature of the upper surface and a significant downward curvature of the lower surface, with a larger displacement at the tip compared to the first mode. A small 3D coordinate system with x, y, and z axes is shown at the bottom left of the mode shape.
$\lambda_3 = 198.6$ Hz	 The eigenmode shape for $\lambda_3 = 198.6$ Hz shows a cross-section of a tapered beam with a central cutout. The beam is oriented horizontally. The mode shape is characterized by a slight upward curvature of the upper surface and a slight downward curvature of the lower surface, with a small displacement at the tip. A small 3D coordinate system with x, y, and z axes is shown at the bottom left of the mode shape.
$\lambda_4 = 323.5$ Hz	 The eigenmode shape for $\lambda_4 = 323.5$ Hz shows a cross-section of a tapered beam with a central cutout. The beam is oriented horizontally. The mode shape is characterized by a significant upward curvature of the upper surface and a significant downward curvature of the lower surface, with a larger displacement at the tip compared to the second mode. A small 3D coordinate system with x, y, and z axes is shown at the bottom left of the mode shape.

Table B.2: The eigenfrequencies and modes in the case where the actuator input is fixed

Eigenfrequency $\mu_i$	Eigenmode
$\mu_1 = 71.3 \text{ Hz}$	
$\mu_2 = 197.3 \text{ Hz}$	
$\mu_3 = 322.6 \text{ Hz}$	
$\mu_4 = 393.5 \text{ Hz}$	

## Appendix C

# Experimental images

Below, the output shapes of the prototype, as compared to print-outs of the different expected shapes can be found. It can be seen that the deviation from the expected shapes gets bigger, when the total amount of deformation is increased.



Figure C.1: Neutral position

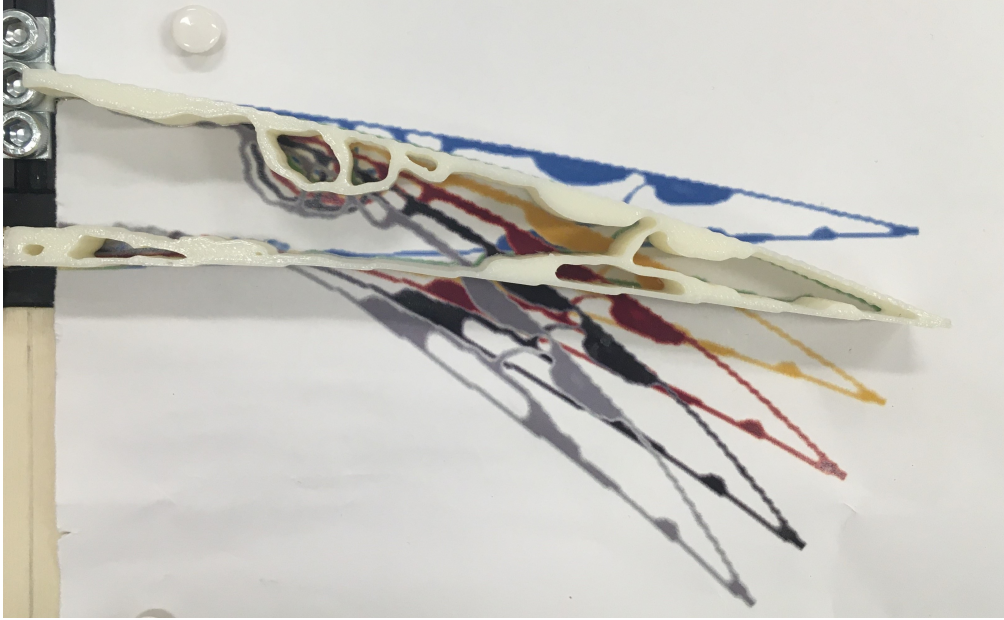


Figure C.2: 1st (green) deformed position

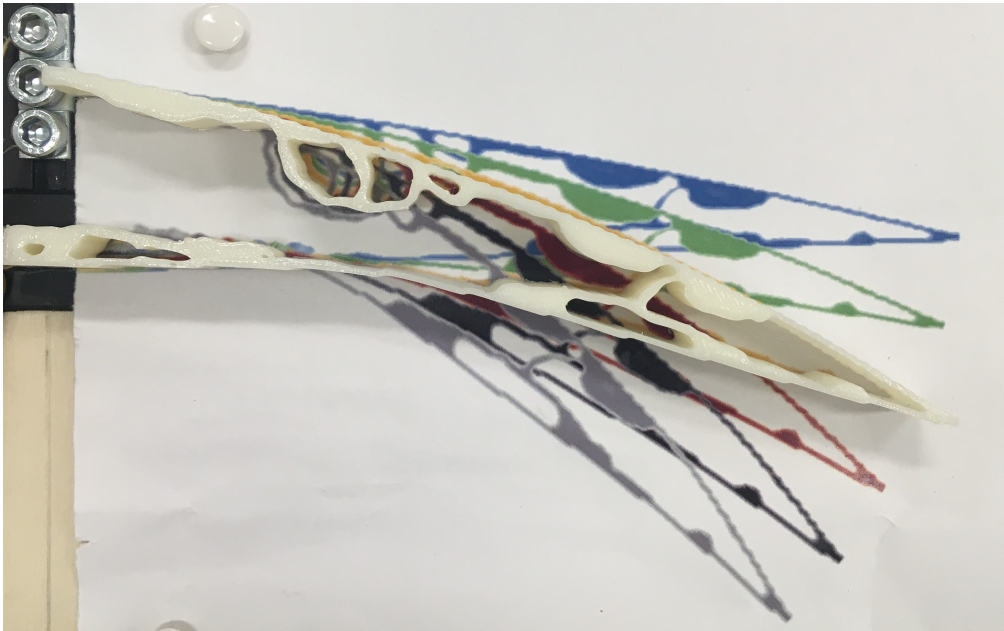


Figure C.3: 2nd (yellow) deformed position

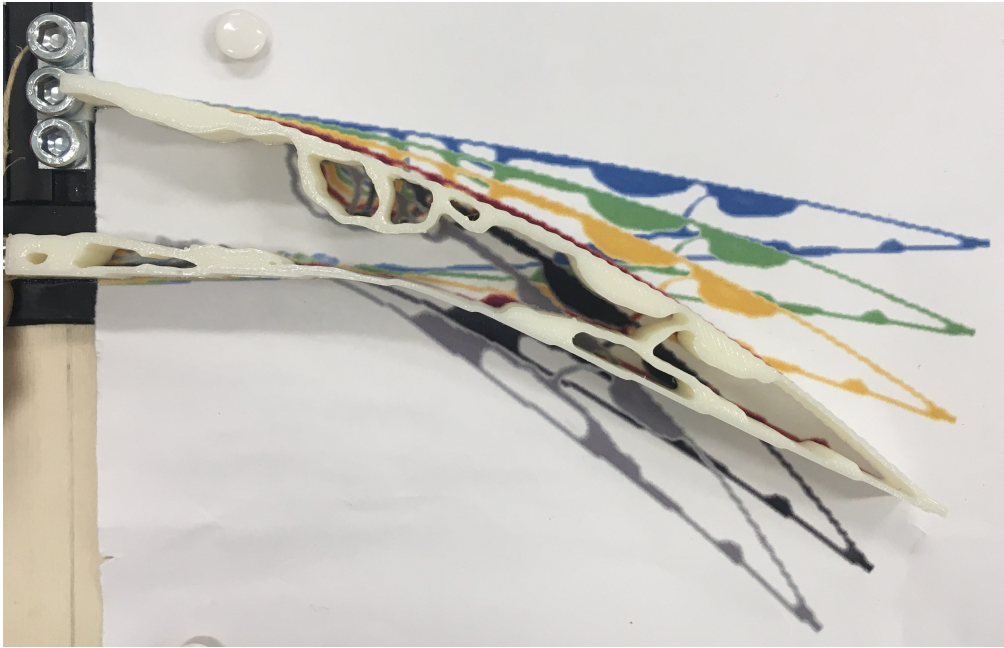


Figure C.4: 3rd (red) deformed position

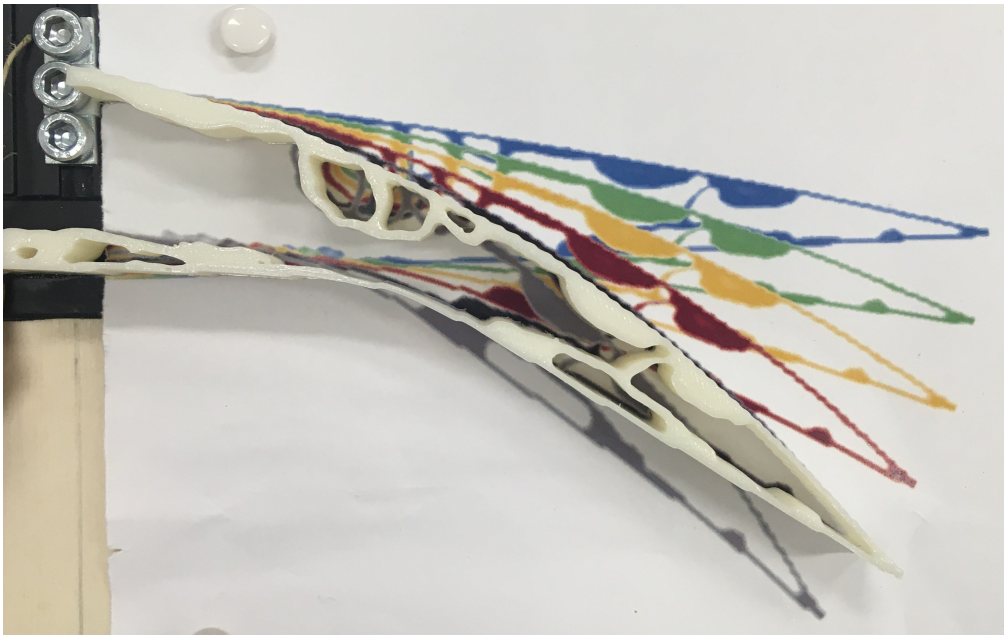


Figure C.5: 4th (black) deformed position

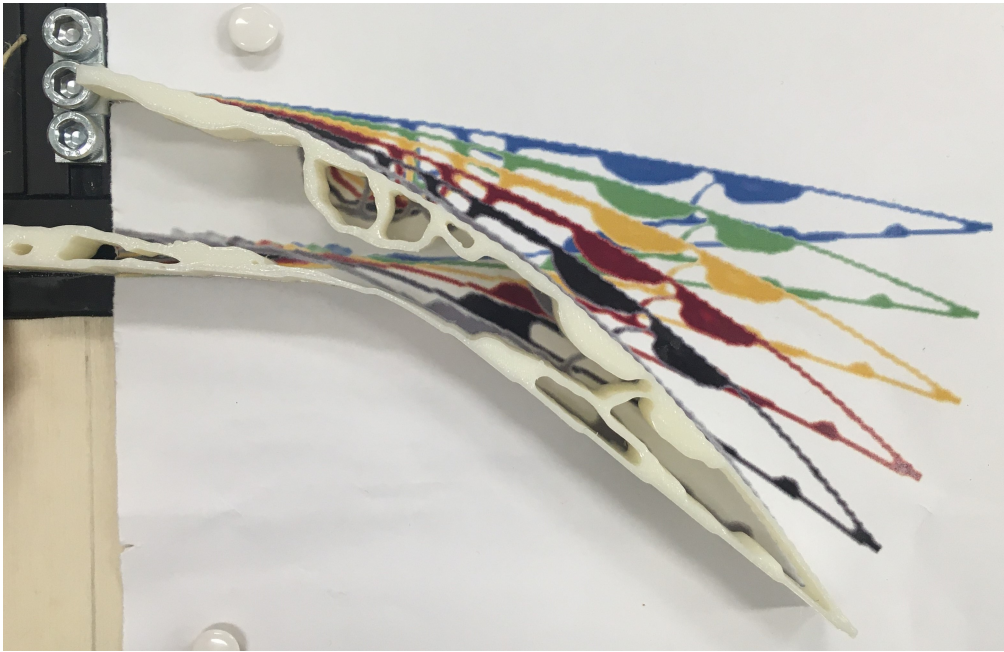


Figure C.6: 5th (grey) deformed position